# RESEARCH ARTICLE

**Key Points:**
- Nonisentropic mixing is measured for a variety of baroclinic wave life cycles
- Nonisentropic irreversible mixing is highly localized and clearly structured
- Climatological stratification leads to maximum stratosphere-troposphere Exchange

**Correspondence to:**
Y. H. Yamazaki,
hiro.yamazaki@ncl.ac.uk

# Spatiotemporal development of irreversible mixing in midlatitude baroclinic wave life cycles: Morphology, energetics, and nonisentropic mixing activity

## Y. H. Yamazaki[1] and W. R. Peltier[2]

[1]School of Geography, Politics and Sociology, University of Newcastle upon Tyne, Newcastle upon Tyne, UK, [2]Department of Physics, University of Toronto, Toronto, Ontario, Canada

**Abstract** The significance of nonisentropic irreversible mixing processes is diagnosed for idealized simulations of synoptic-scale baroclinic wave life cycles along the subtropical jet stream, using a nonhydrostatic, anelastic, mesoscale model subject to a free-slip surface boundary condition. A variety of morphological features of mixing is identified such as a mesoscale columnar vortex associated with the onset of frontal fracture, episodic overturnings along the surface fronts, "wrinkling" of the tropopause, and injection of tropospheric air into the stratosphere. The evolution of the degree of nonisentropic irreversible mixing is first analyzed by computing the change of the "base" component of potential energy that cannot be converted into kinetic energy. The structure of the mixing activity is also diagnosed through inspection of spatiotemporal changes of entropy to demonstrate that the surface fronts are by far the most active regions of such activity. This activity is found to be primarily longitudinal, extending from the surface to the lower stratosphere, to form a three-dimensional spiral in the synoptic-scale cyclone and along the fronts. However, an exceptional region also exists along the warm front, where the structure becomes primarily transverse in the mature phase of frontal development in a model including an explicit representation of small-scale turbulence. In all simulations, the net transfer of mass and heat across the tropopause is from troposphere to stratosphere. The maximum transfer occurs when the observed climatological level of stratification contrast is assumed between stratosphere and troposphere. The same climatological choice leads to a minimum net irreversible mixing, which occurs primarily at Earth's surface.

## 1. Introduction

Knowledge of the extent and importance of irreversible mixing processes is essential to understanding the high Reynolds number flow of a stratified fluid. Both the atmosphere and oceans of Earth are strongly stratified and naturally support a variety of phenomena through which mixing is engendered. One of the most fully investigated of such natural processes and one that has a striking impact on the general circulation of the atmosphere is the process of baroclinic wave evolution at the synoptic scale. Whereas the dominant mechanism underlying the initial growth is well explained by the classical analyses of *Charney* [1947] and *Eady* [1949], the mechanisms of nonlinear saturation and decay processes are still under active investigation [*Polvani and Esler*, 2007; *Moon and Feldstein*, 2009; *Nakamura and Solomon*, 2011]. These phases of wave evolution involve both synoptic-scale processes related to wave mean flow interaction and mesoscale processes including the generation of both localized secondary instabilities and the excitation of internal gravity waves through imbalance [*Ley and Peltier*, 1978; *Bush et al.*, 1995; *O'Sullivan and Dunkerton*, 1995; *Molemaker et al.*, 2005; *Plougonven and Snyder*, 2007]. Even smaller-scale processes involving strong dissipation and irreversible mixing will inevitably be induced by baroclinic wave life cycles along the tropospheric fronts and tropopause, both of which engender mesoscale and smaller-scale processes in regions in which the temperature and velocity fields develop strong spatial gradients and which, by occurring, prevent the development of spatial singularities in these otherwise adiabatic nondissipative fields.

For example, a conceptual model by *Shapiro and Keyser* [1990] and *Neiman et al.* [1993] emphasizes the importance of frontal fracture and the westward bent warm front, which presumably involves the development of such small-scale processes. In fact, *Polvani and Esler* [2007] have performed an analysis of idealized baroclinic wave life cycles for the two canonical baroclinic life cycle "flavors," commonly referred to as LC1 and LC2, originally identified by *Simmons and Hoskins* [1977, 1978] and clearly characterized by *Thorncroft et al.* [1993]. Moreover, *Kunz et al.* [2009] investigated the impact of changes of the stratosphere on

the evolutions of the LC1 and LC2 life cycles. Meanwhile, a thorough recent review of the variety of processes and interactions that occur between the upper troposphere and lower stratosphere in such events is that provided by *Gettelman et al.* [2011].

In the context of recent and projected climate changes, plausible variations of extratropical cyclone structure are of particular interest. For example, *Geng and Sugi* [2003] have investigated the impacts of increased greenhouse gases and anthropogenic aerosols on midlatitude baroclinic waves using comprehensive global general circulation models, and *Castanheira et al.* [2009] have described the observed increase of baroclinicity in the upper troposphere and lower stratosphere under these changing conditions.

One of the goals of this paper is to identify the morphological features of irreversible nonisentropic mixing and to estimate the importance of the mesoscale processes that emerge during the nonlinear evolution of the synoptic-scale disturbance in the framework of a nonhydrostatic cloud-scale model from which moist processes as well as a explicit parameterization of the turbulent surface boundary layer have been eliminated. Our purpose in performing detailed analysis of an idealized model of this kind is to provide a benchmark study against which the results obtained using more elaborate models may be compared. In this context we will examine the influence of the assumed strength of the subgrid-scale turbulent diffusivity as well as the magnitude of stratospheric stratification on the mesoscale features that develop during the course of typical synoptic-scale life cycles. The dynamical framework employed for the purpose of these analyses is a nonhydrostatic model based on the anelastic approximation [*Clark*, 1977], which has previously been demonstrated to successfully simulate various subsynoptic-scale features of interest [*Polavarapu and Peltier*, 1990, 1993; *Bush and Peltier*, 1994; *Yamazaki and Peltier*, 2001, hereafter YP]. We have elected to return to this model in order to fully connect the current work to that previously performed. Therefore, we will not incorporate the most recent developments of models from which sound waves have been filtered such as those by *Lilly* [1996] and *Arakawa and Konor* [2009]. For present purposes, we expect that these enhancements of the anelastic dynamical framework will be of second order in importance.

A further goal of the present work will be to quantitatively describe the spatiotemporal development of nonisentropic irreversible mixing that is associated with deformations of the surface fronts and tropopause by employing rigorous measures of this process which differ from those that have previously been brought to bear on this fundamental problem. We will discuss several different methodologies that may be employed to measure the degree of irreversible mixing that occurs during the spatiotemporal evolution of a stratified fluid undergoing the synoptic-scale baroclinic instability process. *Nakamura* [1996] proposed one such methodology, and thereby triggered a variety of spatially explicit mixing analyses. His idea was that the mixing rate could be estimated by the equivalent length of an appropriate tracer contour, multiplied by an appropriate diffusion coefficient. This measure is especially useful when the diffusivity is uniform and isotropic, and it can be usefully employed to describe the spatial distribution of the mixing rate. However, in a complex system such as a planetary atmosphere or ocean, the effective diffusivity is a function of time, space, and sampling resolution and cannot be determined on an a priori basis. Nevertheless, *Haynes and Shuckburgh* [2000a, 2000b] employed a reanalysis model to determine effective diffusivity and successfully diagnosed the mixing in the stratosphere and in the vicinity of tropopause. Meanwhile, *Nakamura* [2001] further elaborated a mathematical framework that can be employed for the analysis and diagnosis of mixing processes.

Also, in the context of the atmospheric system, *Patmore and Toumi* [2006] employed an entropy-based measure of mixing at the tropopause to analyze satellite-based observational data. A further successful methodology that has been employed to quantify the temporal evolution of nonisentropic mixing has been accomplished by following the original analysis by *Margules* [1903], who employed a two-box model to define a partition of the potential energy into two subcomponents, which respectively can and cannot be converted into kinetic energy [see also *Gill*, 1982]. *Lorenz* [1955] clarified the meaning of these energy components and established the concept of available potential energy (APE hereafter) and minimal potential energy (we will refer to the latter as "background" or "base" potential energy, or simply BPE). BPE is the part of the potential energy that cannot be transformed into kinetic energy and can be understood as the part of the potential energy that reflects only the thermodynamic state of the fluid as a whole.

In the context of mixing analyses in a narrow Scottish lake, *Thorpe* [1977] carried out a thorough inspection of observed density profiles. His analysis included inspection of "stable" density profiles, which were obtained by sorting the measured data on which the observed density profile was based. This procedure forms the first

step in the methodology that must be implemented to compute BPE. The concepts of APE and BPE were also employed by *Winters et al.* [1995] to quantify the evolving degree of diapycnal mixing that occurs in a shear flow undergoing two-dimensional Kelvin-Helmholtz instability. More recently, *Caulfield and Peltier* [2000] employed a variant of the same procedure to diagnose the evolution of irreversible mixing during the three-dimensional "life cycle" of a stratified shear flow undergoing Kelvin-Helmholtz instability. This methodology has also been employed to demonstrate the nonmonotonic dependence of the mixing efficiency on the strength of the density stratification in such flows [*Peltier and Caulfield*, 2003]. Recent analyses of higher-resolution 3-D direct numerical simulations (DNSs) by *Mashayek and Peltier* [2012a, 2012b, 2013] have further revealed the presence of a "zoo" of secondary small-scale instabilities that are responsible for irreversible mixing and which, on account of the variation of their strength as a function of Richardson number, explain the nonmonotonicity of the variation of mixing efficiency with increase in this parameter.

In the oceans the issue of the inference of an appropriate turbulent diapycnal diffusivity has always been considered to be far more central than is the case for atmospheric applications as the small-scale processes through which this diffusivity is engendered act directly on the large-scale thermohaline overturning circulation. For example, *Munk* [1966] and *Munk and Wunsch* [1998] demonstrate through an analysis of the abyssal circulation that a diapycnal diffusivity of magnitude $10^{-4}\,\mathrm{m^2/s}$ is required to close the energy budget of the ocean circulation. Very recently, *Mashayek and Peltier* [2012a, 2012b, 2013] have shown, through detailed DNS analyses of high Reynolds number shear-induced stratified turbulence, that this number is quite accurately recovered on the basis of the *Osborn* [1980] model which assumes that the turbulence is not only stationary but also isotropic and fully developed. In that case, however, the assumptions of the *Osborn* [1980] model were shown to be significantly violated in the range of Richardson numbers in which the mixing efficiency decreases as a function of increasing Richardson number [see also *Caulfield and Peltier*, 2000; *Peltier and Caulfield*, 2003; *Mashayek et al.*, 2013]. This effect has been shown to explain the nonmonotonic variation of mixing efficiency with Richardson number as commented above.

In this paper, we will initially employ the idea introduced by *Margules* [1903], which has been more recently applied to numerical models of incompressible flow in the *Boussinesq* [1903] approximation by *Winters et al.* [1995] and *Caulfield and Peltier* [2000]. This procedure will be extended herein so that it can be applied to the more atmospherically realistic anelastic, compressible fluid models characterized by either isentropic or nonisentropic reference states. In addition, an alternative methodology for the analysis of irreversible mixing will also be proposed. We will demonstrate that the evolution of classical thermodynamic entropy is closely related to the evolution of BPE and define an irreversible activity index ($I_{IA}$) to diagnose the temporal and spatial localization of irreversible processes.

After a brief description of our model of baroclinic wave development in section 2, the results of a series of numerical simulations of baroclinic wave life cycles will be presented in section 3. The energy-based diagnosis employed to quantify irreversible nonisentropic mixing will then be discussed and applied in section 4. The entropy-based analysis will then be employed to describe the mixing activity in both time and space in section 5. We will also discuss the net transfer of mass and enthalpy across the tropopause that takes place during the life cycle of a single baroclinic wave in section 6. Our results are summarized in section 7 where we will reiterate the limitations of the analyses performed in which neither moist processes nor those associated with the turbulent surface boundary layer are included.

## 2. The Model of Baroclinic Wave Development

The numerical model to be employed for all of the analyses herein is based on an implementation of the equations describing a nonhydrostatic anelastic fluid. The governing equations were discretized using second-order accurate-centered finite differences, as described in *Clark* [1977]. In a rotating Cartesian coordinate system $\boldsymbol{x} = (x, y, z)$ with $x$ increasing eastward, $y$ northward, and $z$ upward, the governing equations can be written as

$$\frac{\mathrm{D}\boldsymbol{u}}{\mathrm{D}t} + \boldsymbol{f} \times \boldsymbol{u} = \nabla\frac{p_1}{\rho_0} - \frac{\theta_1}{\theta_0}\boldsymbol{g} + \boldsymbol{F}, \tag{1}$$

$$\frac{c_p}{\theta_0}\frac{\mathrm{D}\theta}{\mathrm{D}t} = \frac{Q}{T_0}, \tag{2}$$

$$\nabla \cdot (\rho_0 \boldsymbol{u}) = 0. \tag{3}$$

**Table 1.** Constants Employed in the Definition of the Basic State Potential Temperature Field

| Constants | Definition | Values | Units |
|---|---|---|---|
| $\theta_0$ | Reference state potential temperature | 273.587 | K |
| $g$ | Gravitational acceleration | 9.81 | $m\,s^{-2}$ |
| $f$ | Coriolis parameter | $10^{-4}$ | $s^{-1}$ |

in which $\boldsymbol{u} = (\,u(\boldsymbol{x}, t), v(\boldsymbol{x}, t), w(\boldsymbol{x}, t)\,)$ is three-dimensional velocity vector, $p = p(\boldsymbol{x}, t)$ is pressure, $\theta = \theta(\boldsymbol{x}, t)$ is potential temperature, $\rho = \rho(\boldsymbol{x}, t)$ is density, and $T = T(\boldsymbol{x}, t)$ is absolute temperature. The vector $\boldsymbol{F}$ denotes the frictional force per unit mass, while the scalar $Q$ denotes the rate of heating due to turbulent thermal diffusivity. The vector $\boldsymbol{f} = (0, 0, f)$ is the Coriolis parameter, and $\boldsymbol{g} = (0, 0, -g)$ is the acceleration due to gravity, the values of which are set equal to the constant values listed in Table 1. The subscript 0 denotes a corresponding quantity in the reference state, all of which are functions of height only, whereas the subscript 1 denotes a deviation from the reference state. The reference state is assumed to be motionless and isentropic in the analyses to follow.

We will be obliged to consider two sources of dissipation in the numerical model, one due to the numerical methodology, $\boldsymbol{F}_N$, and the other due to the explicit turbulence parameterization, $\boldsymbol{F}_T$, which does not include that in the surface boundary layer. Hence, we have

$$\boldsymbol{F} \equiv \boldsymbol{F}_N + \boldsymbol{F}_T. \tag{4}$$

The friction arising from the numerical methodology, $\boldsymbol{F}_N$, is introduced primarily to ensure numerical stability, and the mathematical forms selected for the numerical viscosity may be classified into three groups: namely, those having $\nabla_H^6$, $\nabla_H^4$, and $\nabla_H^2$ dependencies, where $\nabla_H^2$ denotes the horizontal Laplacian operator. The numerical viscosity of $\nabla_H^6$ type is employed over the entire domain except for a few grid planes near the north and south walls, where the lower order diffusion operators are applied.

The explicit parameterization of friction that is intended to represent the influence of unresolved "turbulence" at the subgrid scale is $\boldsymbol{F}_T$. We employ a three-dimensional version of the first-order closure discussed by *Lilly* [1962]. The turbulent mixing coefficient, $K_m$, is a function of an external constant that we will refer to as the "eddy viscosity" parameter $K_C$, the deformation Def, and the local gradient Richardson number $R_i^*$, as

$$K_m = \begin{cases} K_C - \text{Def}\left(1 - R_i^*\right)^{1/2}, & R_i^* < 1; \\ 0, & \text{otherwise}; \end{cases} \tag{5}$$

Further details are available in *Clark* [1977]. The eddy Prandtl number for the turbulence parameterization is assumed to be in unity, and there is no parameterized boundary layer near the surface as previously stated. We employ a free-slip boundary condition at the bottom of the simulation domain for simplicity, and to enable us to provide a benchmark case in comparison to which the results obtained for various boundary layer parameterizations may be compared in later work. The energetics of the model may be summarized as follows:

$$\frac{d}{dt}\text{TKE} = <\text{VHS}> - <\text{DIS}> \tag{6}$$

$$\frac{d}{dt}\text{TPE} = - <\text{VHS}> - <\text{DIF}> \tag{7}$$

$$\frac{d}{dt}\text{ZKE} = <\text{VRS}> - <\text{HRS}> - <\text{DIS}_Z> \tag{8}$$

$$\frac{d}{dt}\text{EKE} = <\text{VHS}> - <\text{VRS}> + <\text{HRS}> - <\text{DIS}_E> \tag{9}$$

where $<>$ denotes an average over the entire domain. Detailed definitions of these terms are provided in YP. The energy components TKE and TPE are total kinetic energy and total potential energy, respectively, and ZKE and EKE are the zonal mean and eddy components of kinetic energy, respectively. The energy conversion terms on the right-hand sides of the equations are vertical heat flux (VHF), vertical Reynolds stress (VRS), horizontal Reynolds stress (HRS), dissipation (DIS), and diffusion (DIF). The dissipation is partitioned further into the zonal mean and eddy components ($\text{DIS}_Z$ and $\text{DIS}_E$), and the total energy due to dissipation is assumed to be lost from the system.
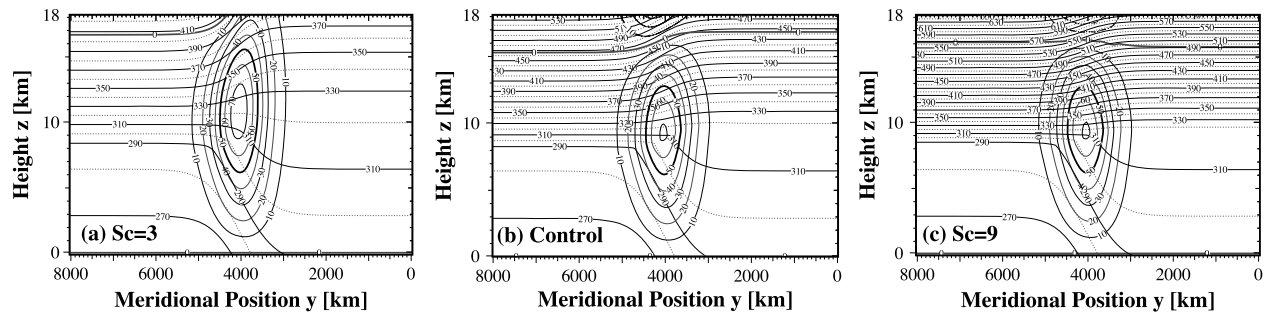
**Figure 1.** The initial fields in terms of the distribution of potential temperature (thin lines) and zonal winds (thick lines) with different choices of the stratification contrast between stratosphere and troposphere, The cases for (a) $S_C = 3$, (b) 6, and (c) 9. The Control case (Figure 1b) corresponds closely to the climatology for winter conditions of the subtropical jet stream in the western Pacific as discussed in *Yamazaki and Peltier* [2001].

### 2.1. Initial Fields

We will employ three primary initial flows in a cyclic channel, each of which consists of modeled troposphere and stratosphere with different degrees of stratification, as displayed in Figure 1. The flow fields of the control case shown in Figure 1b were constructed to represent a realistic midlatitude jet stream observed in wintertime in the western Pacific. The potential temperature distribution is analytically defined as described in YP. The potential temperature is continuous across the tropopause although there exists a jump in its vertical gradient. The channel length, width, and height are taken to be 4000 km, 8000 km, and 18 km, respectively.

For the present investigation, the strength of the stratification of the stratosphere is controlled by a new parameter that we will refer to as the stratification contrast, $S_C$, namely,

$$N_S^2 \equiv S_C N_T^2, \qquad (10)$$

where $N_S^2$ denotes the squared buoyancy frequency of the stratosphere and $N_T^2$ denotes that of the troposphere ($N_T^2 \equiv 10^{-4}\,\mathrm{s}^{-1}$ for the present applications). Also employed is an initial flow with a rigid lid at the modeled tropopause ($z = 9$ km), which is expected to represent the case with infinitely large stratification contrast. The initial zonal velocity $U(y, z)$ is set to be zero on the ground and is calculated in the overlying region such that it satisfies the thermal wind balance relationship. Both cross-frontal and vertical components of the initial velocity are identically zero over the entire domain.

This definition of the initial mean flow is identical to that which was employed by YP when $S_C = 6$. In the present model, the height of the tropopause, $h_T$, is fixed when $S_C$ is equal to or less than 6 and the cross-frontal change of tropopause height decreases monotonically as $S_C$ increases above 6, as

$$h_T \equiv h_0 - \frac{g}{\max\left(N_S^2, 6N_T^2\right)} \cdot \frac{\theta_J}{\theta_c} \tanh\left\{\frac{(y - y_C)w_J}{Y_J}\right\}. \qquad (11)$$

All other parameters are the same as those described in YP.

Moreover, we will also discuss some aspects of results from simulations with two additional initial flows in the same channel geometry as the control: one with reduced baroclinicity (similar to the climatological zonal mean) in section 3.1.1 and the other with slightly reduced stratospheric stratification ($S_C = 4$) in section 4. The meridional cross sections for zonal velocity and potential temperature are also shown on Figure 1. Both cross-frontal and vertical components of the initial velocity are identically zero over the entire domain. Other characteristic values are summarized in Table 1.

## 3. Overview of the Simulated Life Cycles

We have therefore carried out six primary numerical experiments, the conditions for which are summarized in Table 2. The experiments may be seen to separate into two groups: namely, those designed to test the

**Table 2.** Summary of Simulation Conditions: $K_C$ Is the Eddy Mixing Parameter and $N_S^2$ Is Static Stability of the Stratosphere[a]

| Run | $K_C$ (m$^2$ s$^{-1}$) | $N_S^2$ (s$^{-1}$) |
|---|---|---|
| Control | 0 | $6 \times 10^{-4}$ |
| LowNs | - | $3 \times 10^{-4}$ |
| HighNs | - | $9 \times 10^{-4}$ |
| RigidLid | - | $\infty$ |
| Eddy1 | $10^2$ | - |
| Eddy2 | $10^3$ | - |

[a]Dash denotes the same as Control.

influence of the assumed strength of the subgrid-scale turbulence ($K_C$) and those designed to test the impact of the choice of the stratification contrast between troposphere and stratosphere ($S_C$).

All of the parameters of the control run, labeled "Control," are the same as those of the single synoptic-scale simulation reported previously in YP. However, for the purpose of the present study we have developed a more accurate method for calculating the initial state of balance. The time step employed in these simulations is 90 s, and the numerical grid spacing are DX = 62.5 km in the along-front direction, DY = 63.5 km in the cross-front direction, and DZ = 310 m in the vertical direction. No turbulence parameterization was incorporated in Control except for the constant hyperdiffusion described in the previous section, and no disturbance is explicitly superimposed on the balanced initial fields. A small-amplitude baroclinic disturbance inevitably develops out of the truncation error and assumes the optimal modal structure. Although unperturbed initialization may fail to capture the fastest growing mode of linear theory in principle and requires a longer period of numerical integration in practice, such simulations have been shown to better resolve the early stage of exponential growth as previously demonstrated in YP and *Yamazaki et al.* [2004].

In order to examine the dependence of the baroclinic wave life cycle on the strength of upper level stratification, we have performed two comparison analyses labeled HighNs and LowNs, which respectively employ more and less strongly stratified stratospheres as noted in Table 2. The initial fields for these runs have been illustrated in Figure 1. On physical grounds, it would be reasonable to expect that a different degree of upper level stratification will lead to a different degree of tropopause deformation because this property of the structure relates to the effective rigidity of the tropopause interface.

The cases Eddy1 and Eddy2 are the same as Control except that the turbulence parameterization is activated at different strengths. As discussed by *Lilly* [1962], the external eddy viscosity parameter, $K_C$, can be interpreted to be determined by the choice of characteristic grid scale $\triangle$ and the Kolmogorov number $k_K$ as $K_C = (k_K \triangle)^2$, where $\triangle = (\text{DX DY DZ})^{1/3}$. In the viscous simulations, the Kolmogorov numbers that correspond to Eddy1 and Eddy2 are approximately 0.009 and 0.03, respectively. Thus, the parameterized eddy mixing effects can be considered weak for all cases.

### 3.1. The Control Run

In this section, the general features of the life cycle that is simulated by our control run, Control, will be briefly summarized. Since an almost identical case was previously described in YP, the discussion herein will be restricted to the characteristics of the flow in the nonlinear stage of the life cycle, focusing primarily on the morphological features related to active mixing.

### 3.1.1. Energetics

The evolution of Control is summarized in terms of its energetics in Figure 2. For the first 9 days, the formation of a normal mode disturbance takes place, followed by distinctive exponential growth. The growth rate decreases in the saturation period from day 13.5 to day 15.0, and the period of decay lasts from day 15.0 to day 17.5.

The evolution is almost identical to the results described in YP except that we are now able to recognize an even earlier phase of the exponential growth at smaller amplitude due to the improvements in the procedure for obtaining the balanced initial state. Unlike the initial fields employed by YP, the temperature field for the present study is calculated from the analytical definition at the desired resolution while the velocity field is directly calculated by an accurate discrete implementation of thermal wind balance on a staggered grid without iterative modification.

This level of care is required because the conventional figures concerning the energy exchanges are often misleading, without explicit illustrations of growth rate changes. One important point we wish to draw attention to in Figure 2 is that the initiation and termination of exponential growth occur at day 9 and day 13, respectively. In other words, inspection of the change of growth rate such as Figure 2c is crucial to identify the impacts of mesoscale events in the baroclinic wave life cycle.
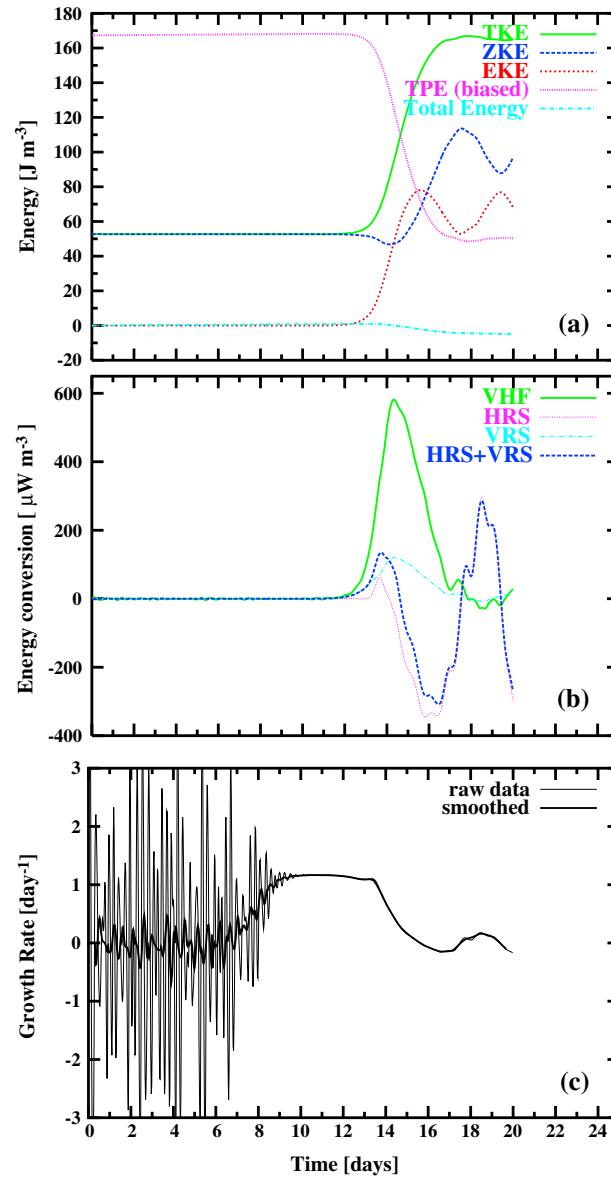
**Figure 2.** Evolution of (a) energy components, (b) energy convergence terms, and (c) the growth rate for the Control run. The smoothed curve in Figure 2c is obtained as a weighted running mean.

The initial fields of conventional life cycle simulations are not well balanced due to the presence of a superimposed disturbance. This makes the analysis of the termination of the exponential growth stage and of the initial stage of saturation difficult, simply because the stage of truly "exponential" growth is hard to identify [e.g., *Bush and Peltier*, 1994]. The first stage of nonlinear saturation (i.e., from the termination of exponential growth to the beginning of decay) is characterized by the saturation of the positive energy terms themselves (Vertical Heat Flux, VHF, and Vertical Reynolds Stress, VRS), which no longer grow exponentially from day 13.5 to day 15. In the evolution of the energy conversion terms shown in Figure 2b, the beginning of the saturation period coincides with the emergence of a positive impulse of Horizontal Reynolds Stress, HRS. In other words, the onset of saturation is *not* due to simple barotropic decay. Instead, it is triggered by barotropic growth of a new disturbance in our model, which leads thereafter into the conventionally recognized phase of barotropic decay.

### 3.1.2. Evolution of the Surface Front

The evolution of the surface potential temperature field is displayed in Figures 3f–3j as a time series of plan view snapshots. Despite the absence of the initially superimposed disturbance, a normal mode disturbance with zonally sinusoidal structure initially develops. The strong influence of nonlinear effects becomes evident by day 13.75 with the formation of a cusp near the fracture point of the frontal structure. The cusp develops until approximately day 15.75 when it is detached from the front as previously discussed in *Polavarapu and Peltier* [1993].

During the development of the cusp in our simulations, parallel-banded structures, which resemble often observed "frontal rain bands," form along the warm and cold fronts as seen in Figure 3h. Similar structures have been observed in the simulations of *Polavarapu and Peltier* [1990], *Bush and Peltier* [1994], and YP as well as a preliminary higher-resolution numerical experiment, which employed half-grid spacing and time step, and an identical configuration to *Bush and Peltier* [1994] in all other respects. In particular, *Bush et al.* [1995] have analyzed the evolving imbalance and suspected that this structure might be due to either the generation of internal gravity waves, which are trapped by the front, or a spurious consequence of insufficient vertical resolution. The present analysis finds that the increase of vertical resolution has minor influence. Instead, the scale length of the structure is strongly dependent on the horizontal resolution. The longitudinal structure can also be due to the emergence of symmetric instability, as discussed by *Raymond* [1978], *Bennetts and Hoskins* [1979], and *Emanuel* [1979, 1988], and the presence of negative potential vorticity along the warm front supports this hypothesis.
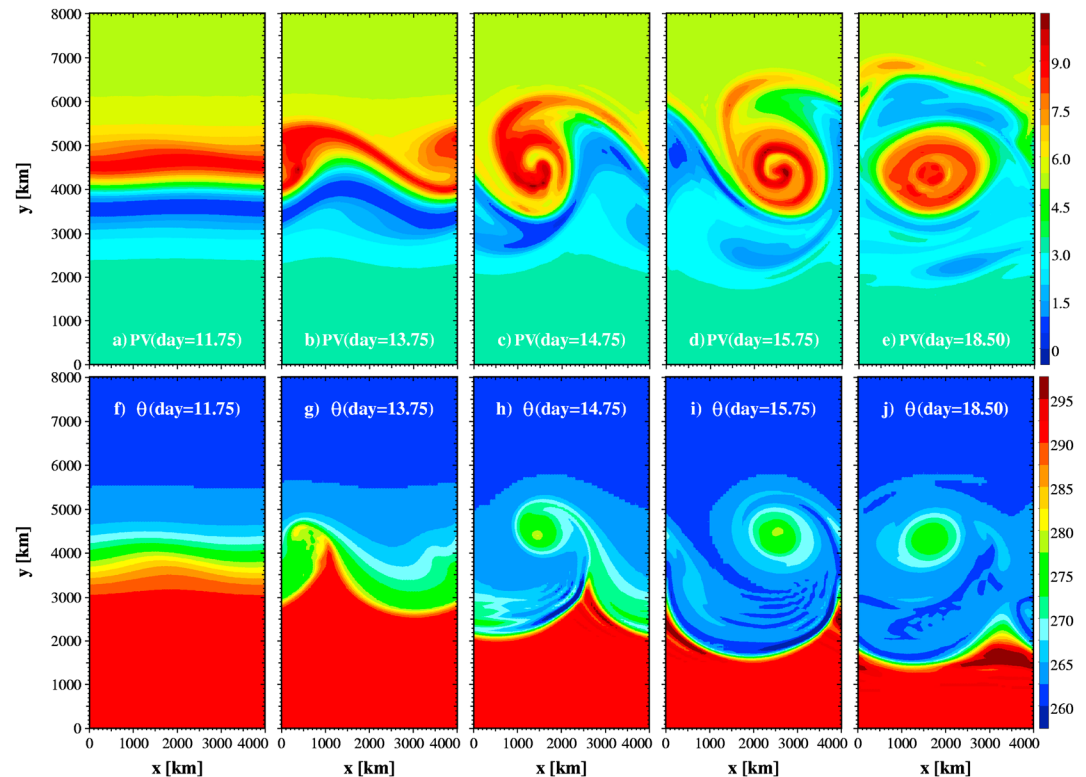
**Figure 3.** Upper and surface cyclogeneis from Control: Successive plan view snapshots show (a–e) potential vorticity along the surface with PV = 325 K, near the tropopause (see Figure 1b), and (f–j) surface potential temperature.

### 3.1.3. Upper Level Cyclogenesis

Isentropic potential vorticity (PV) maps [*Hoskins et al.,* 1985] on the $\theta = 325$ K surface are employed to diagnose the features of the lower stratosphere that are associated with upper level cyclogenesis. This surface is initially located just above the tropopause and goes through the core of the jet [see *Yamazaki and Peltier*, 2001, Figure 1c]. Note, however, that this isentropic surface does not necessarily represent the conventionally defined tropopause and deforms considerably and assumes a "wavy" structure by day 14.

The evolution of the PV field on this isentropic surface is shown in Figures 3a–3e. A weak sinusoidal variation of an initially parallel structure becomes visible by day 11, and the wavy pattern becomes clearly nonsymmetric by day 12.5. At approximately day 13.5, a small region of high PV appears to the north of the front near the western boundary of the simulation domain, as seen in Figure 3b. This is associated with the barotropic development of frontal fracture as is clear on the basis of Figure 2b. Clear signs of this highly localized structure of the barotropic event is evident in Figures 3b and 3g at $x = 500$ km and $y = 4500$ km.

As the synoptic-scale wave becomes intense and the development strongly nonlinear, an elongated strip of PV begins to evolve into a beautifully articulated spiral structure in our $f$ plane model. The evolution of this spiral structure was first clearly resolved in the analyses of *Polavarapu and Peltier* [1990] and has been investigated in further detail by *Methven and Hoskins* [1998], *Methven* [1998], *Polvani and Esler* [2007], and *Gettelman et al.* [2011].

### 3.1.4. Tropopause Deformation

The tropopause can be approximately represented by the isosurface on which potential vorticity (PV) is in unity as equal to the cases examined by *Bush and Peltier* [1994]. This surface does not exactly overlay the tropopause at the center of the jet and slightly penetrates into the lower stratosphere as shown in YP. Nevertheless, the surface reasonably represents the initial tropopause, and the conservative property of PV in adiabatic inviscid flow implies that by observing the deformation of this isosurface, it may effectively allow us to visualize the deforming tropopause without having to explicitly introduce a field of passive tracers. Please note, however, that this definition is different from the conventional definition of the tropopause, which is defined in terms of lapse rate [*World Meteorological Organization*, 1957].
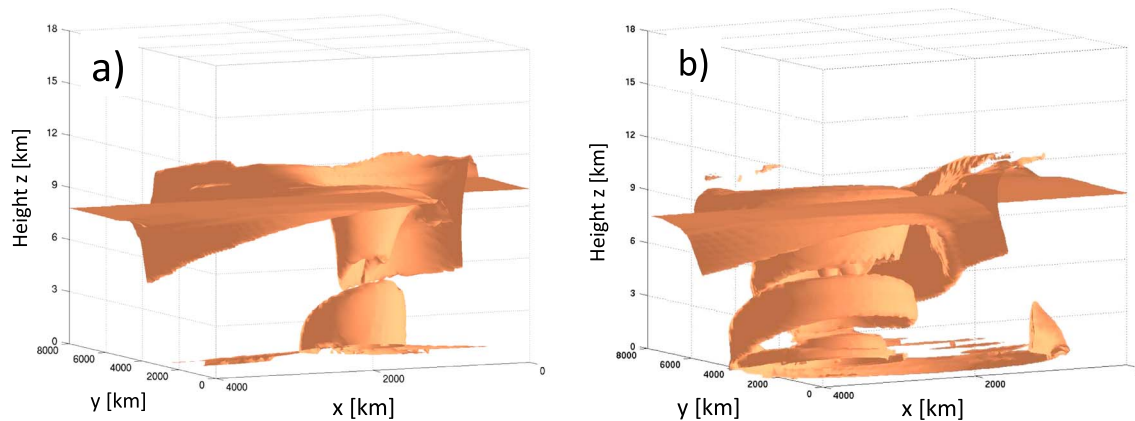
**Figure 4.** Three-dimensional deformation of the tropopause: The isosurface with PV = 1 PVU from Control is rendered at model days (a) 14.25 and (b) 15.75. The viewpoint is northwest of the simulation domain for the eastward mean flow.

Two examples of the three-dimensional structure of the tropopause, which is defined by this isosurface, are visualized in Figure 4. The figure clearly shows the complexity of the three-dimensional structure of this isosurface. The isosurface rendering in this figure actually shows one surface that represents the deformed tropopause and another that shows the region of high PV, generated near the bottom boundary. Until day 14.25, as illustrated in Figure 4b, the deformed tropopause can easily be distinguished from the surface of boundary-generated PV. However, by day 15.75, the descending tropopause apparently intertwines with the ascending surface of boundary-generated PV, and it becomes impossible to distinguish between the two isosurfaces solely by inspecting the structure from a few points of view. For example, we had to examine several cross sections for day 15.75 to actually tell that the two major isosurfaces shown in Figure 4b are separated.

An interesting feature in Figure 4b is the existence of a region of overturning and nearby fragmentary structure in the vicinity of the edge of the upward ridge of the deformed tropopause. The fragments originate from a larger upward pointing finger of low-PV air located near the entrance to the region of depressed tropopause. The top view of the isosurface (not shown) revealed that the upward finger is the most prominent element of the "tropopause wrinkles" which have elongated structure along the upper front running parallel to the jet streak. A similar structure to this upward pointing "tropopause finger" has been observed during the North Pacific Experiment project as an upward and backward burst of the jet stream [*Langland et al.*, 1999].

Whereas *Wang and Polvani* [2011] investigated the formation of a double-tropopause event, *Añel et al.* [2012] examined the origin of the air mass enclosed between different parts of the folded tropopause. Meanwhile, *Chen et al.* [2013] very recently discussed an example in which a particularly deep development of the near-surface turbulent boundary layer occurred. Similar features are readily recognized in our highly idealized model of the atmosphere that includes neither an explicit water cycle nor surface friction.

It is clear that the analysis of a single-rendered isosurface does not provide a suitable basis on which to perform quantitative comparisons of the degree of tropopause deformation during cyclogenesis. We will rather diagnose the deformed tropopause primarily on cross sections of the PV field along the central axis of the initial jet (at $y = 4000$ km) as the spatial migration of the jet is insignificant during the life cycle. The evolution of the nonlinear wave in terms of a selected set of such PV cross sections is displayed in Figure 5. Illustrated in Figure 5a is the PV structure of the nonlinear wave that exists when the amplitude of the "synoptic-scale deformation" of the tropopause has obtained its maximum expression. The nonsymmetric shape of the synoptic-scale deformation reveals some evidence of upper level saturation by day 13.75 in the form of a broad basin-shaped depression of the tropopause. It is interesting to note that the saturation of the upper level deformation of the "lid" coincides with the saturation of the impulse of positive barotropic conversion of energy. Meanwhile, the underside of the synoptic-scale deformation, which is defined by the lower part of the roof of the troposphere, is visible near $x = 3700$ km. The amplitude of the synoptic-scale deformation will be measured as the difference between these two heights in section 3.2.2.
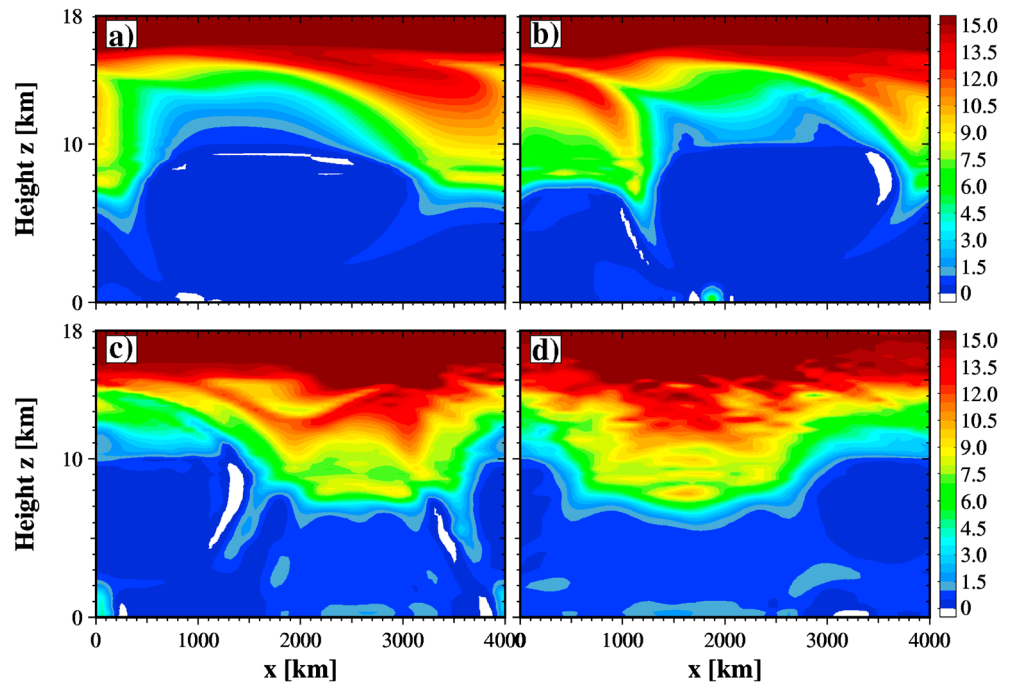
**Figure 5.** Evolution of the vertical PV structure along $y = 4000$ km for the case Control. The times for which data are shown are (a) 13.75, (b) 14.25, (c) 15.75, and (d) 18.5 days.

Aside from the large horizontal-scale deformation of the tropopause, these figures also reveal the continuing descent of stratospheric air in a small-scale "fold" (see Figures 5b and 5c), as well as the development of secondary folds associated with the spiral structure of the main vortex (Figure 5c). Structures very similar to these are, of course, observed in nature [e.g., see *Danielsen and Hipskind*, 1980], but we must remember that Figure 5c shows only a single cross section through what is, in fact, the complex three-dimensional structure of tropopause deformation shown previously in Figure 4. The final PV structure shown in Figure 5d for day 18.5 is smoother in the troposphere but is a more fragmented, layered-pancake-like structure in the stratosphere.

### 3.2. Influence of the Strength of Subgrid-Scale Turbulence

The influence of the assumed level of subgrid-scale turbulence on these simulations has been investigated by varying the eddy viscosity parameter $K_C$ in the turbulen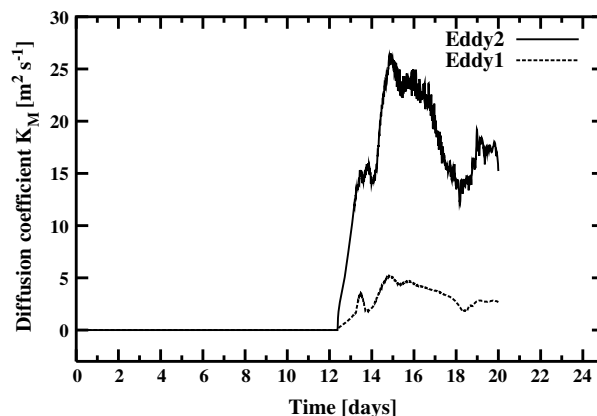ce parameterization. In this section, this influence will be examined on the basis of conventional diagnoses of the model fields. The value for the Control case is zero for all time, but the value changes according to equation (5) for other cases as a function of both time and space.

The evolution of the spatial maximum of $K_m$ is illustrated in Figure 6 for cases Eddy1 and Eddy2. Until day 12.375, the parameterized turbulence effects remain identically zero because the local Richardson number has remained in excess of unity everywhere in the domain. The initial impulse of strong mixing at day 13.5 corresponds to the time of onset of positive horizontal Reynolds stress. This supports
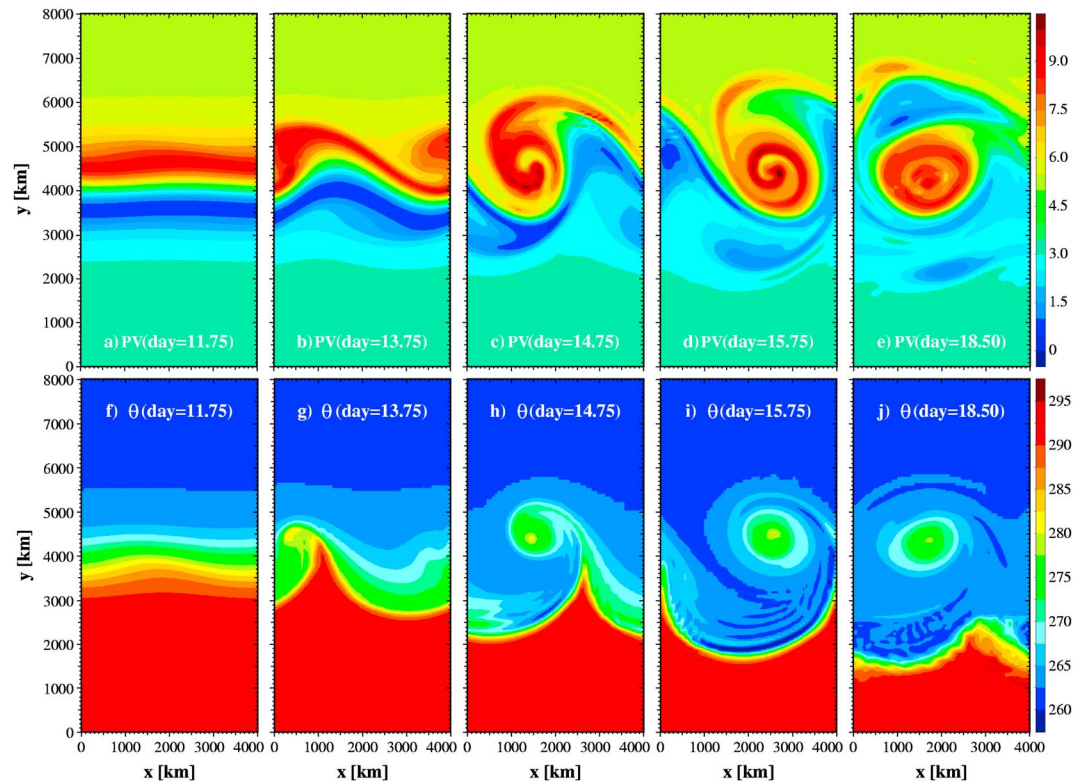


**Figure 6.** Spatial maximum of the Richardson number-dependent mixing coefficient $K_m$ described in equation (5).

**Figure 7.** The same as Figure 3, for the run-denoted Eddy2.

the view that the frontal fracture accompanies a strong increase in diffusivity. Moreover, the very noisy evolution for the entire period suggests the occurrence of numerous mixing events which are short lived and, most probably, highly localized.

The energetics of run Eddy2 is almost identical to those of Control although minor differences can be identified in the evolution of the energy conversion terms. More significant differences will be evaluated through mixing analyses in sections 4, 5, and 6.

### 3.2.1. Upper and Lower Level Cyclogenesis

The evolution of the surface potential temperature field is, in general, similar for all cases with different levels of subgrid-scale turbulence. The evolution of Eddy2 is displayed in Figures 7f–7j which can be compared with Figures 4f–4j. The similarity includes the mesoscale features such as "multiple fronts" that can be identified as the parallel structure along both warm and cold fronts that are most clearly seen at days 14.75 and 15.75.

Nevertheless, in the evolution of Eddy2, a clear sign of intense mixing becomes apparent along the fronts by day 15.75, subsequent to which the fronts become more diffuse. The first sign of mixing along the warm front appeared around day 15 as evidenced by the emergence of a periodic structure that is perpendicular to the front. This structure is clearly visualized in Figure 7i for day 15.75. Although this could be a consequence of numerical under resolution, it is worth noting that radar observations of warm fronts have identified a strikingly similar structure, which is explained as a consequence of Kelvin-Helmholtz instability [*Chapman and Browning*, 1997, 1999]. We have confirmed that the Richardson number in this region is less than 0.25 in our simulation, which therefore supports this interpretation.

Meanwhile, through airborne observations of the Fronts and Atlantic Storm-Track Experiment cyclone Intensive Observation Period 11, *Wakimoto and Bosart* [2001] also identified the occurrence of the same perpendicular structure in the warm frontal region. They have further identified the existence of a periodic structure that runs parallel to the warm front in the along-front average of the cross-frontal vertical cross sections. Based upon their results, the coexistence of the parallel and perpendicular structures supports the existence of a checkered structure revealed in Figure 7i. The mature cold front shown in Figure 7j is not
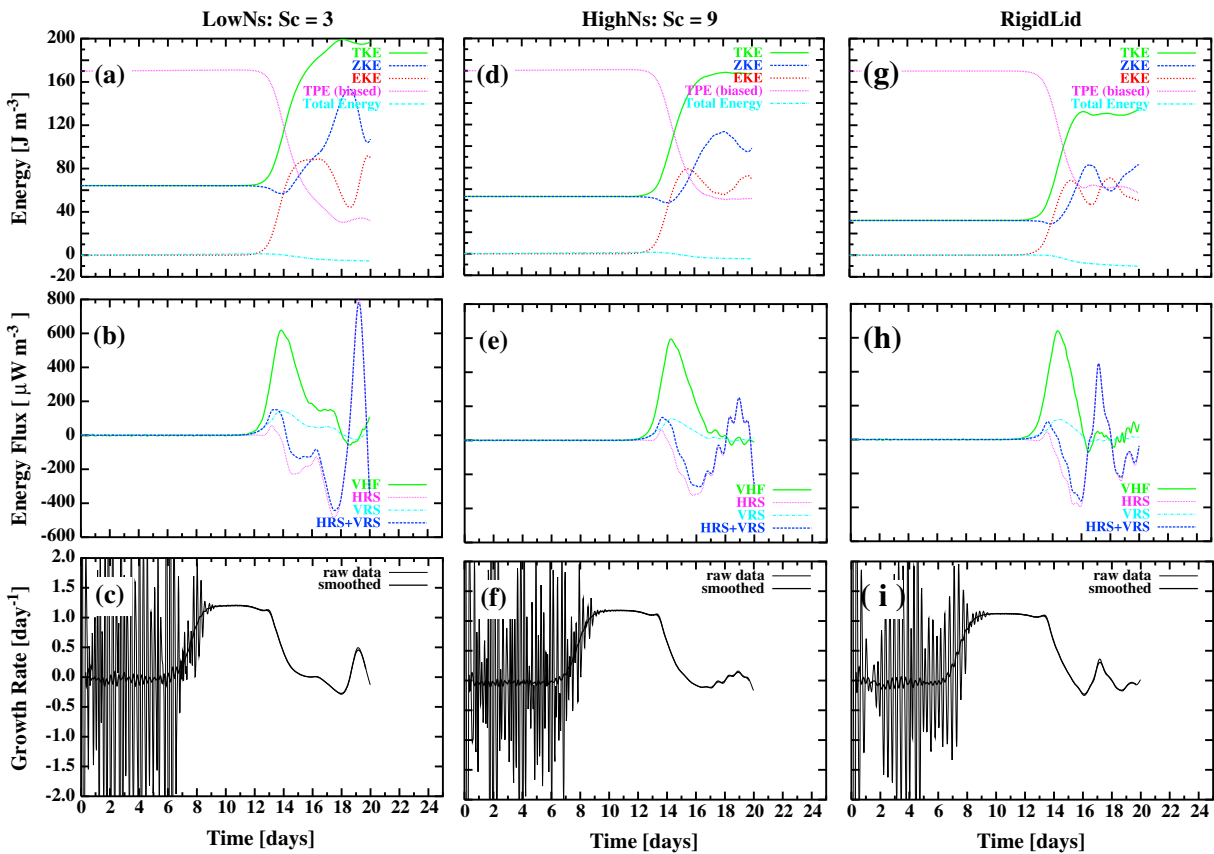
**Figure 8.** Energetics as a function of the stratification contrast, $S_C$. (a–f) The same convention is used as Figures 2a–2c but for $S_C = 3$ and 9. (g–i) The RigidLid run placed a rigid upper boundary at $z = 9$ km to represent the case with effectively infinite stratification contrast.

smooth but rather wavy. The observed wavy structure reported by Wakimoto and Bosart is of 20 km scale and, of course, our model cannot fully resolve such fine structure. Although, the viscous theory of free shear instability predicts an increase of the wavelength of the most unstable waves in our model with strong eddy viscosity, and the wavelength of the periodic features are represented by more than two grid points, we cannot fully dismiss the possibility that these structures are of numerical origin. Further ultrahigh resolution analyses will be required to resolve this issue.

Despite the marked difference at the surface, the evolution of the upper level cyclogenesis diagnosed on the isentropic PV maps is almost identical for all cases with different levels of parameterized diffusion. Examples are presented in Figures 7a–7e for Eddy2.

### 3.2.2. Vertical Structure of PV

The evolution of the vertical cross section of PV is generally similar to that for Control as previously shown in Figure 5a. The maximum level of synoptic-scale deformation of the tropopause at day 13.75 is identical to that of Control. At day 14.25, when the degree of tropopause descent reaches the initial temporal maximum, the region of strong PV gradient in the stratosphere near $(x, z) \approx (3000 \text{ km}, 12 \text{ km})$ shows a sign of "wrinkles" or "ripples" with similar amplitude. An investigation of the horizontal structure revealed that the wrinkles run primarily parallel to the jet streak, supporting the possible occurrence of a symmetric instability. However, the effects of increased viscosity are most evident near the surface. The region of high PV along the front is smaller in Eddy2 than in Control. At day 15.75, when the descent of the folds reaches the secondary temporal maximum, the small-scale PV structure in the troposphere is slightly but significantly smoother than that of Control. The disappearance of small-scale structure indicates signs of irreversible nonisentropic mixing having occurred. The final PV structure at day 18.5, compared with that from Control, shows a stronger influence of tropospheric mixing, although most of the fine structure in the stratosphere remains unaffected.
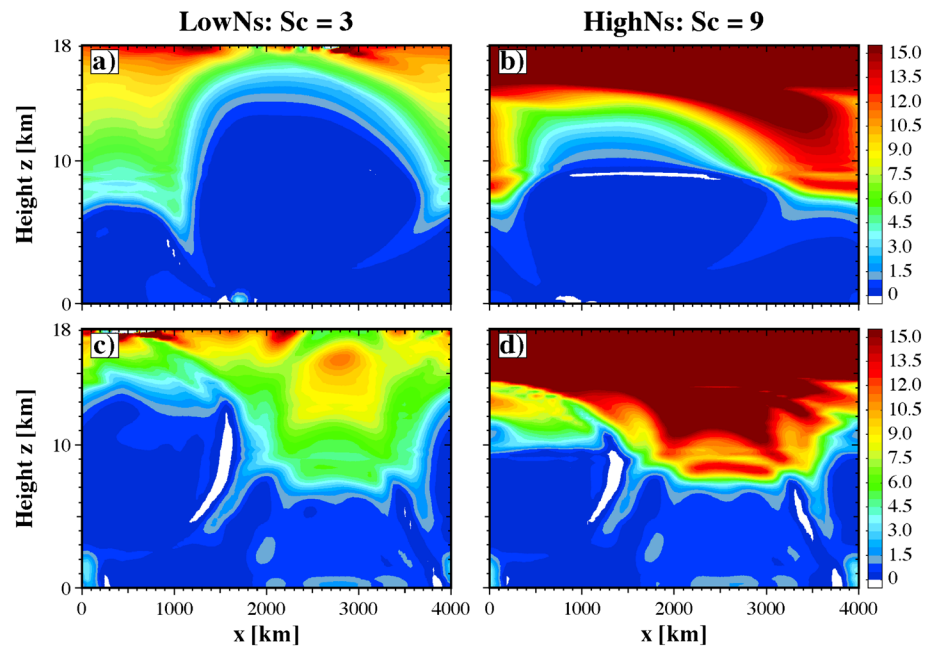
**Figure 9.** Tropopause deformation, diagnosed using the cross section of potential vorticity along $y = 4000$ km, for (a and c) $S_C = 3$ and (b and d) 9. Figures 9a–9d are directly comparable to Figures 5a and 5c, respectively.

### 3.3. The Influence of the Stratification Contrast

The influence of the varying stratification contrast between stratosphere and troposphere, $S_C$, is investigated in this section by examining the simulated life cycles in flows with different degrees of upper level stratification. The authors are not aware of the existence of similar analyses in the literature.

#### 3.3.1. Energetics

The energetics of the LowNs, HighNs, and RigidLid simulations are summarized in Figure 8. For all cases, results are similar to those obtained in Control. In particular, the growth rate in the exponential stage is essentially independent of the variation in the stratification contrast. This similarity is understandable on the basis of the spatial distribution of the energy conversions during the exponentially growing stage, which occur almost entirely in the troposphere even when the stratification contrast $S_C$ is reduced.

Closer inspection of the energetics does, however, allow us to identify a number of differences. The most notable difference concerns the level of the zonal kinetic energy in the saturated state, which decreases as the stratification contrast increases in Figures 8a, 8d, and 8g. Another recognizable difference concerns the fast oscillatory change of the energy conversion terms. The amplitude and the period of this variation are very sensitive to the stratification contrast, and the oscillatory variation is clearest in the case of HighNs (Figure 8e). A similar oscillatory variation is also evident in the results from the Control and Eddy2 runs, shown in Figure 2.

#### 3.3.2. Deformation of the Tropopause

Examination of the potential vorticity structures delivered by these simulations immediately leads to identification of the most significant differences in the degree of upward penetration of the tropopause at the synoptic scale. Shown in Figures 9a and 9b are the vertical cross sections of the potential vorticity fields when the amplitude of the synoptic-scale deformation, defined in section 3.1.4, is maximum. The maximum amplitude of the deformation increases as the stratification contrast $S_C$ is reduced from that of the control run as expected. The influence of increased stratification contrast is minor because the amplitude of the deformation is already small for the realistic case of Control.

Meanwhile, the maximum degree of descent of the subsynoptic-scale tropopause folds may be diagnosed in Figures 9c and 9d. Despite the strong dependence of the synoptic-scale deformation on the stratification contrast in Figures 9a and 9b, the behavior of the small-scale folds are practically insensitive to the change of the stratification contrast. In fact, the small-scale PV structure in the troposphere below 9 km in height is almost identical for all cases, although the PV structure is completely different in the stratosphere.
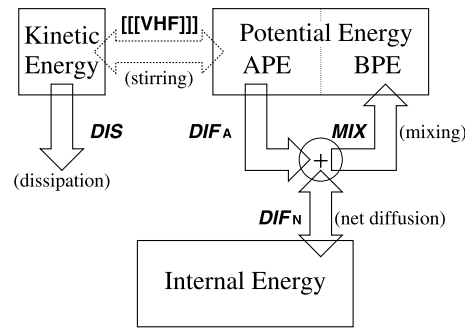
**Figure 10.** Schematics of energy components and the energy conversion terms.

# 4. Energy-Based Diagnosis of Irreversible Mixing

In this section, in order to quantify the extent of irreversible mixing that occurs during the development of a typical baroclinic wave, we will first discuss the concept of mixing rate, the definition of which is based upon the concept of "base potential energy" (BPE) discussed in section 1. The suite of simulated life cycles will then be diagnosed using the measure of irreversible mixing in sections 4.2 and 4.3. In the cyclogenetic process, mixing also occurs isentropically. However, we will focus on the irreversible mixing of the potential temperature field, which is equivalent to the diapycnal mixing that is so important to the understanding of the large-scale dynamics of the oceans, under the more general and atmospherically relevant anelastic approximation.

## 4.1. Mixing, Stirring, and Diffusion

If we are to discuss the diapycnal mixing of initially distinct air masses, we clearly need to have an unambiguous definition of mixing. Our focus in the discussion will be on what is generally termed "irreversible mixing" which excludes simple "stirring." Stirring is the process that occurs during energy conversion from kinetic energy to available potential energy (APE) through buoyancy flux (VHF). Stirring simply involves the adiabatic redistribution of fluid elements, and it is therefore reversible. It is particularly important to realize that stretching of a material interface does not increase the degree of mixing, i.e., the degree to which the entire system is homogenized. The deformation of a material interface can be achieved simply by rearranging the fluid parcels in the system.

The definition of irreversible mixing that we will employ herein relies on the concept of a background or base part of the potential energy as in *Winters et al.* [1995], *Caulfield and Peltier* [2000], and *Peltier and Caulfield* [2003]. The base potential energy (BPE) is the fraction of the total potential energy that cannot be released by any adiabatic rearrangement of fluid parcels. Mathematically, BPE can be defined as the smallest achievable value of the total potential energy that can be reached by any adiabatic redistribution of fluid elements over the entire domain. It is apparent from this definition that no adiabatic process can change BPE, and thus, the evolution of BPE represents the consequence of irreversible mixing without any contribution from (reversible) stirring. Therefore, we will refer to the rate of increase of BPE as a "nonisentropic mixing rate" or simply "mixing rate"

$$\text{MIX}(t) = \frac{\text{d}}{\text{d}t}\text{BPE}(t). \tag{12}$$

Once the value of BPE is obtained, APE can be calculated as the difference between the total potential energy (TPE) and BPE. The net diffusion ($\text{DIF}_N$) is defined as the domain integral of the energy conversion from internal energy (IE) to TPE. The concepts introduced herein are described schematically in Figure 10. Note that under the anelastic approximation, the internal energy works only as a passive reservoir.

The net diffusion is often simply termed "diffusion," and can be expressed for our model as

$$\text{DIF}_N \equiv \langle \text{DIF} \rangle = \frac{g}{\theta_0} \langle z\nabla \cdot (\rho_0 K_m)\nabla\theta \rangle. \tag{13}$$

In the cases of mixing analyses of shear flows undergoing Kelvin-Helmholtz instability in the *Boussinesq* [1903] approximation, the net diffusion can be evaluated entirely on the basis of the integral over the top and bottom boundaries and is essentially constant. Therefore, the net diffusion in this case can easily be interpreted as the steady increase of potential energy due to the presence of the background stratification whereas the mixing is an enhanced homogenization as the consequence of stretched contour lines, which in turn is due to the breaking of the Kelvin-Helmholtz billow. Our case is more complex, and the net diffusion changes significantly, primarily because strong activity occurs along the lower boundary of the model

domain. Of course, in a more complex model that included a parameterization of the turbulent surface boundary layer this would be significantly modified.

Another irreversible energy conversion term, defined by the conversion from the kinetic energy (KE) to IE, is often called "viscous energy conversion," which consists of "momentum dissipation" (loss of KE) and "viscous heating" (gain of IE). A conventional scaling argument concludes that such viscous heating is insignificant, and it is thus excluded from our numerical model.

### 4.2. Calculation of Base Potential Energy for the Anelastic Model

A direct method to calculate BPE was described in *Winters et al.* [1995] for a 2-D model and generalized by *Caulfield and Peltier* [2000] and *Peltier and Caulfield* [2003] for 3-D models, all under the Boussinesq approximation. These procedures consist of three steps: (I) sorting of fluid elements according to density, (II) stable layering of fluid elements, and (III) computation of the total potential energy.

For a generalized anelastic system (GAS), which employs either an isentropic or a nonisentropic reference state, we find that the calculation of BPE becomes slightly more elaborate due to its "modeled compressibility." Under the Boussinesq approximation, density, temperature, and potential temperature are all conserved for any adiabatic displacement of a fluid element. However, it is potential temperature that is conserved in a GAS. We therefore use the potential temperature for the sorting of fluid elements (step I).

The second step required is the flattening and layering of the fluid elements. This step is also generalized for a GAS to take into account the modeled compressibility. The thickness of each layer must be calculated to satisfy the modeled compressibility that is consistent with the approximate conservation of mass. This can be stated for a small fluid element of volume $\delta V$ as

$$\rho_0(z)\delta V = \text{const.} \tag{14}$$

This is obtained by ignoring the first-order terms in $\rho_1/\rho_0$ under the generalized anelastic approximation. In other words, in all anelastic models with uniform or nonuniform reference density, the adiabatic vertical displacement of a fluid element changes the density in accord with the density profile of the assumed reference state.

For the same reason, the volume of the fluid element changes following equation (14). Therefore, the final state after the rearrangement of fluid elements consists of a stably stratified stack of thin layers of fluid with unequal thickness.

Once the adiabatic layered state has been computed, we employ the usual definition of the total potential energy to calculate the potential energy of the rearranged state, namely,

$$\text{PE}_G \equiv -\int_V \rho_0(z)gz\frac{\theta_1(x,t)}{\theta_0(z)}dV. \tag{15}$$

### 4.3. Evolution of Base Potential Energy and Mixing Rate

Evolution of the total and base potential energy is displayed in Figure 11a for Eddy2. The difference between these two curves represents the available potential energy. The net gain of BPE during the main life cycle (from day 9 to day 17.75) of Eddy2 is only 6% of the loss of total potential energy. In other words, the energy conversions that occur during the apparently dramatic event of a baroclinic wave life cycle in our model are essentially reversible in so far as the thermodynamic changes are concerned.

The evolution of BPE is summarized in Figure 11b for all cases with different model parameters. The influence of the stratification contrast, $S_C$, is minor. However, it is interesting to note that the increase of BPE is not a monotonic function of the stratification contrast. At day 18, for example, the BPE is smallest when $S_C=6$ followed by cases with $S_C=4$, $S_C=3$, and $S_C=9$. Note that we have introduced a new run with $S_C=4$, to illustrate the dependence of mixing effects as a function of the stratification contrast.

On the contrary, the strong influence of the assumed level of small-scale turbulence is clearly evident in Figure 11b. The evolution for the case labeled Control clearly shows the impact of the implicit diffusivity due to the discrete numerics of the model, and the rapid mixing during the saturation and decay stages is evident from day 13 to day 17. In this sense, the evolution is very similar to the other cases with explicit parameterization of turbulence except that the mixing is much weaker.
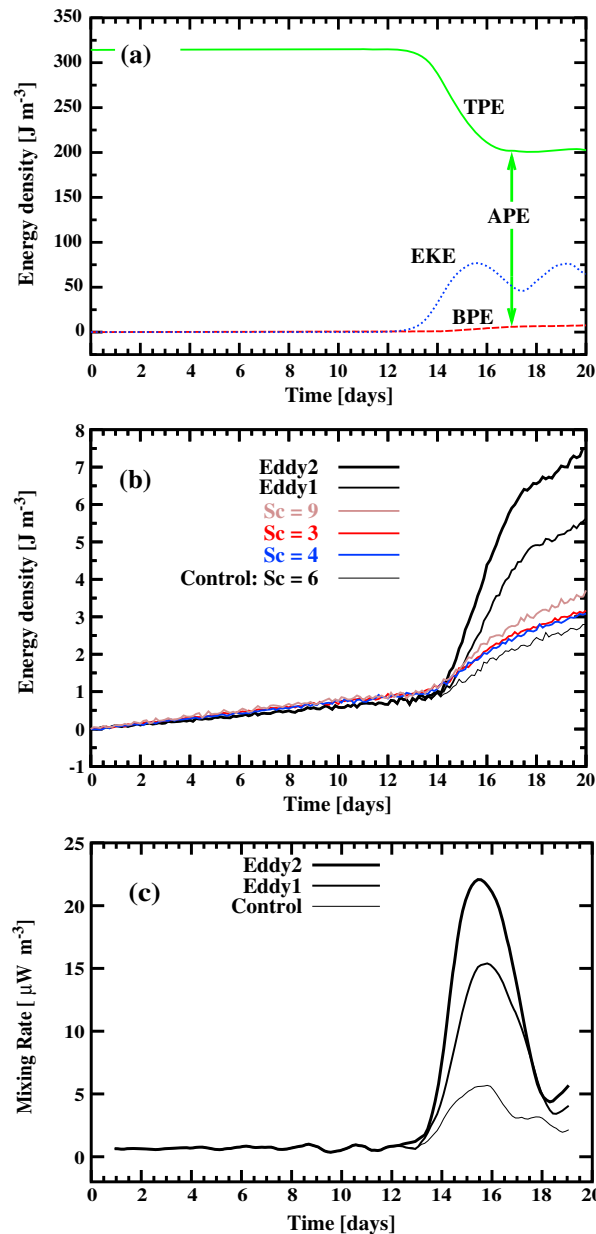
The evolution of the mixing rate, MIX, is summarized in Figure 11c. The maximum mixing rate reaches 22 $\mu W\,m^{-3}$ for case Eddy2, which is achieved at day 15.5 in the early decay stage of the life cycle. This magnitude remains only 4% of the maximum magnitude of the reversible stirring rate (i.e., VHS). Nevertheless, the evolution of irreversible nonisentropic mixing and its dependence on the assumed strength of the turbulence is clearly quantified.

It is also of interest for us to identify the spatial distribution of strong mixing activity. In the context of mixing analysis of a Scottish lake, *Thorpe* [1977] employed the adiabatically rearranged "sorted" profiles. Similarly, in the cases of mixing analyses of Kelvin-Helmholtz instability, *Winters et al.* [1995] and *Caulfield and Peltier* [2000] have demonstrated that the examination of the sorted profiles of the potential temperature is useful in identifying the active region of mixing. These analyses have recently been repeated for much higher Reynolds number flows in *Mashayek and Peltier* [2013].

Displayed in Figure 12a are examples of such sorted profiles of potential temperature before and after the single-life cycle event of Eddy2. It is apparent that the irreversible (nonisentropic) mixing due to the baroclinic life cycle has a very minor smoothing effect even for the case with strongest turbulent viscosity. The only exception, which can be clearly identified in Figure 12, is the cooling of an air mass $(285 < \theta < 295\text{ K})$, which was initially located in the band that extends from the warm side of the surface front to the upper troposphere across the jet, and warming of the cold air near the surface. Although not conclusive, this seems to indicate that the most active mixing takes place along the surface front, which is consistent with the morphological features that we have identified in section 3. Further investigation of the spatial distribution of mixing will be provided in the next section using an alternative measure.

**Figure 11.** Evolution of (a) energy components for Eddy2, (b) base potential energy (BPE) for a variety of runs, and (c) the irreversible mixing rate (MIX) for Control, Eddy1, and Eddy2 runs.

## 5. Entropy-Based Mixing Diagnostics

In this section, the concept of thermal entropy and an associated measure of irreversible mixing is discussed. Following the description of these quantities, the entropy-based diagnosis is applied to the simulated life cycles.

### 5.1. Thermal Entropy and an Irreversible Activity Index

Consideration of the evolving entropy during the baroclinic wave life cycle will aid in describing the development of an irreversible mixing process because it is a direct measure of irreversible processes, in
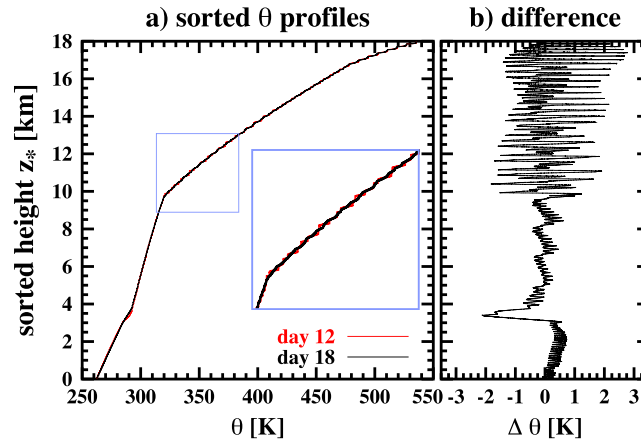
**Figure 12.** Sorted equivalent density: (a) sorted potential temperature profile with magnified inset and (b) the increase of the sorted potential temperature from day 12 to day 18.

general. Here we may simply define a part of the entropy that is solely due to the thermodynamic state of a fluid element by ignoring the presence of motion. We employ this quantity and call it "thermal entropy" or simply entropy in this paper. On the assumption that the contribution of strongly nonequilibrium effects is small for synoptic-scale and mesoscale motion of the lower atmosphere, the entropy will be a useful measure of the development of irreversible processes including mixing.

For example, it is well known [e.g., *Gill*, 1982] that the specific entropy of an ideal gas, $S_G$, in an equilibrium state can be defined as

$$S = \Delta c_p \log\theta + \text{const},\tag{16}$$

where $c_p$ is specific heat capacity and $\theta$ is potential temperature. We set the arbitrary constant to zero for our analysis because our interest is only in the change of entropy. This is our definition of the specific thermal entropy in this paper. In the anelastic approximation, the definition of specific entropy in equation (16) is not affected. However, the equation of mass conservation is approximated as

$$\rho_0(z)\delta V = \text{const},\tag{17}$$

where $\rho_0(z)$ denotes the density profile of the reference state. Therefore, the density in equation (16) should be replaced by the reference state density, which defines the entropy that is precisely conserved for adiabatic processes under the anelastic approximation. Using this definition, we can estimate the total entropy in the whole domain, $S_T(t)$, in terms of the entropy per unit volume as

$$S_T(t) \equiv \frac{\int_V dS_G}{\int_V dV} = \langle \rho_0 s \rangle.\tag{18}$$

Unlike the base potential energy, which was employed in the previous section, entropy is defined locally. Therefore, we may reasonably estimate the spatial distribution of the strength of irreversible (nonisentropic) activity by using the Lagrangian time derivative of the thermal entropy. For an anelastic system, an "irreversible activity index" is thus defined as

$$I_{IA} \equiv \rho_0 \frac{Ds}{Dt} = \rho_0 \frac{D}{Dt} \log\theta.\tag{19}$$

The temporal development and the spatial distribution of the irreversible activity index will reveal quantitatively when and where irreversible processes are taking place. Note that in the anelastic approximation, the buoyancy is measured in terms of the normalized potential temperature anomaly, and thus, the thermal entropy defined in the previous section may also be interpreted as a measure of buoyancy. In fact, the irreversible activity index defined here is proportional to the time derivative of buoyancy in the classical anelastic approximation, namely,

$$I_{IA} \approx \rho_0 c_p \frac{1}{\theta}\frac{D\theta}{Dt} \propto \frac{D}{Dt} \cdot \left(\frac{\theta}{\theta_0}g\right).\tag{20}$$

Moreover, we may also derive a measure of irreversible activity in terms of (the rate of the change of) energy. Since such energy-based analyses are more conventional than those based upon entropy, it might be more useful to employ the diagnostic heating rate (per unit volume) that is defined as

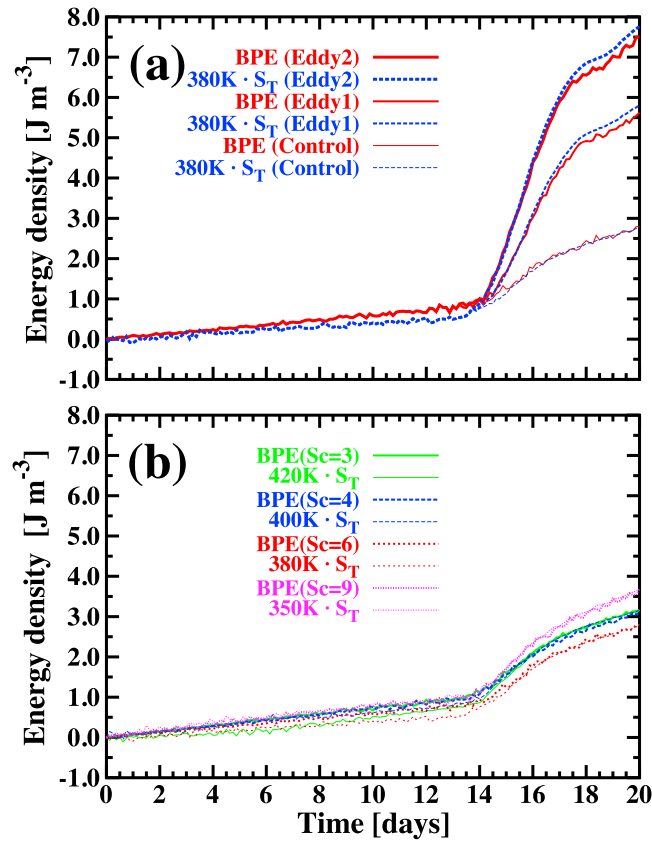$$H_D \equiv \rho_0 T \frac{Ds}{Dt} \approx \frac{c_p \rho_0 T_0}{\theta_0}\frac{D\theta}{Dt}\tag{21}$$

**Figure 13.** Similarity between BPE and entropy for a variety of model runs.

for anelastic models. Note that this quantity is precisely the conventional diabatic heating rate, and that diabatic heating is always associated with irreversibility. However, the irreversible activity represented in this way also includes the impacts of numerical diffusivity. This representation is therefore especially useful for mixing diagnosis.

### 5.2. Evolution of Entropy and Base Potential Energy

The evolution of spatially integrated entropy is summarized in Figure 13 for all cases with different model parameters, together with that of base potential energy (BPE).

The important feature in Figures 13a and 13b is the very good correlation between the increase of BPE and that of the entropy. In fact, the evolution of these two quantities is almost identical when initial biases are removed, and the latter is multiplied by a characteristic temperature, $T^*$, that is empirically obtained for each case. We will not attach any particular physical meaning to this characteristic temperature, but simply note that a monotonic decrease of the characteristic temperature accompanies the increase of the stratification of the stratosphere as stated in the key of Figure 13b. Note especially that a common characteristic temperature is employed in Figure 13a for all cases of Control, Eddy1, and Eddy2, which employ the same initial field.

### 5.3. Vertical Structure of Irreversible Activity

We may next proceed to distinguish the mixing along the tropopause from that which occurs along the surface fronts. Because the mixing rate in section 4 was defined as a scalar quantity for the entire domain, the analysis of the spatial localization of the irreversible mixing was not particularly successful. In contrast, the analysis in section 5.2 demonstrated a strong correlation between the increase of base potential energy and that of domain-integrated entropy. Therefore, the irreversible activity index, discussed in section 5.1, can be used to diagnose the spatial structure of the mixing.

The spatiotemporal evolution of the irreversible activity index was diagnosed from data sets saved every 3 h. In order to ensure that the numerical estimation of the Lagrangian time derivative is accurate, it was explicitly confirmed that the domain integral of the irreversible activity is equal to the time derivative of the domain integral of thermal entropy. This is computationally important because the Lagrangian time derivative of a conservative quantity, such as potential temperature, is the small difference between local time derivative and advection. The advection was computed using a two-point average second-order centered difference scheme, namely,

$$u\frac{\partial s}{\partial x} = \frac{1}{2}\left(u_{i-\frac{1}{2}}\frac{S_i - S_{i-1}}{DX} + u_{i+\frac{1}{2}}\frac{S_{i+1} - S_i}{DX}\right), \tag{22}$$

for the $x$ component.

The zonal mean structure of the irreversible activity was obtained as a horizontal average and is summarized in Figure 14 for Eddy2. The mixing near the tropopause folds is quantified and visualized as well as the even
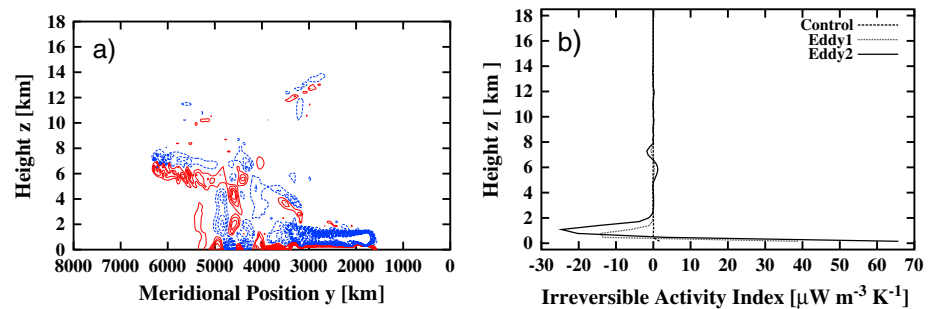
**Figure 14.** (a) Zonal mean irreversible activity index for Eddy2. Red (solid) and blue (dashed) lines indicate positive and negative contours, respectively. Contour levels are from $\pm 5$ to $\pm 100 \, \mu W \, m^{-3} \, K^{-1}$ at $5 \, \mu W \, m^{-3} \, K^{-1}$ intervals, with the higher-value contours omitted for clarity and (b) comparison of the horizontal means of irreversible activity index for Control, Eddy1, and Eddy2 runs.

stronger mixing along the surface (In Figure 14a, contours of high values, which only exist below 2 km in height, are omitted for clarity.). Once more it is important to note that if the model were to include an explicit parameterization of the surface turbulent boundary layer, the results near the lower boundary would be expected to be strongly influenced. Also interesting is the clear evidence of the existence of small regions of active mixing away from the two major regions of mixing. The most notable example exists above the tropopause near $(y, z) = (3000 \, km, 12 \, km)$, which corresponds with the very small peak at 12 km in Figure 14b.

Furthermore, Figures 15a–15c illustrate the 3-D structure of mixing activity. In all horizontal cross sections, the dominant structure generally runs parallel to the flow (i.e., it is longitudinal), which is consistent with the symmetric instability hypothesis. The associated vertical circulation extends from the bottom surface to the lower stratosphere. The spiral cloud bands observed in satellite images may well be a part of this deep longitudinal circulation.

Near the bottom boundary, the horizontal structure at day 13.75 (Figure 15a) reveals the dominance of longitudinal structure and the impact of the frontal fracture. Nevertheless, the emergence of transverse structure can also be recognized along the warm front in later times (Figures 15b and 15c). This transverse activity is consistent with the emergence of Kelvin-Helmholtz instability, which has been observed in the real atmosphere. In our simulation, it becomes more intense as time advances and the mixing associated with the transverse structure becomes dominant by day 15.75. The irreversible activity associated with additional transverse instability can also be identified in the upper troposphere and lower stratosphere. Diagnostics of isentropic PV maps and associated stability analysis have also enabled us to identify a region of small-scale transverse instability. For example, the isentropic PV map shown in Figure 7 indicates transverse periodic anomalies. The irreversible activity in these regions along the upper front clearly illustrates the associated transverse mixing in the predominantly longitudinal activity.

## 6. Net Transfers of Mass and Heat Between Stratosphere and Troposphere

The dramatic event that constitutes a baroclinic wave life cycle with accompanying complex deformation of the tropopause will conceivably involve exchange of mass and heat between stratosphere and troposphere. The evolution of the surface potential temperature field suggested, however, that there exists a dominant region of intense mixing adjacent to the lower boundary. However, as we have commented at every step in our analysis this region is expected to be strongly influenced if explicit incorporation of turbulent surface boundary layer influence were included. Furthermore, the strong dependence of the mixing rate on eddy diffusivity implies that the surface region in our idealized model is more important than that in the vicinity of tropopause, and the entropy-based analyses have confirmed this in section 5.

Here we evaluate the net transfer of mass and enthalpy across the tropopause as the difference between the initial and final state of mass and enthalpy in both stratosphere and troposphere. Although the estimation of the two-way transfer of mass and enthalpy might also be informative, a direct diagnosis of the net transfer will provide useful insight concerning the impact of a single life cycle. A similar analysis was
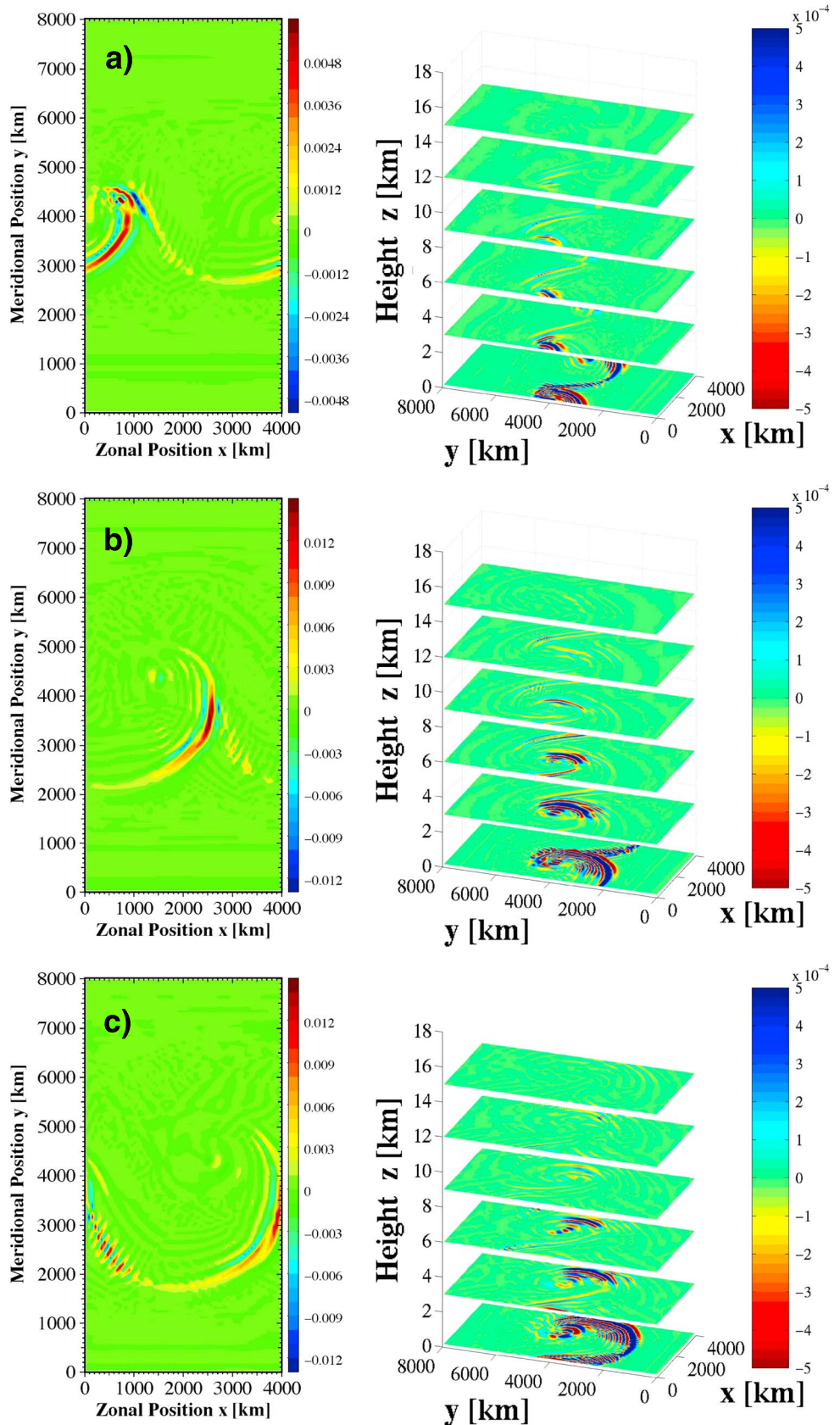
**Figure 15.** Three-dimensional structure of irreversible activity index for Eddy2 run at (a) day = 13.75, (b) 14.75, and (c) 15.75.
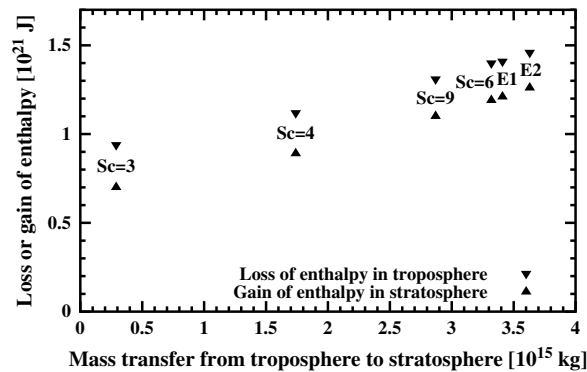
**Figure 16.** Net stratosphere-troposphere exchange of mass and heat for the complete set of simulations. The labels $S_C = 6$, E1, and E2 represent the results from Control, Eddy1, and Eddy2 runs, respectively.

performed by *Lamarque and Hess* [1994] for a simulated tropopause folding event, and a more recent review has been provided by *Stohl et al.* [2003].

Our focus herein is the dependence of the net transfer upon the parameters of the model. The final mass (and enthalpy) of the stratosphere is evaluated at day 18.5 as the mass (and enthalpy) in the region where PV is in excess of 1 potential vorticity unit (PVU) above 3.5 km in height. This definition of the final stratosphere is employed after examining the evolution of the three-dimensional structure of the tropopause, visualized in rendered isosurfaces and in the cross sections of PV. The tropopause structure was inspected from different vantage points for all cases and found to be smooth at day 18.5. Examples of the smooth PV structure are visualized in Figures 3e, 5d, and 7e. Note that an isolated region with high PV does exist below 3.5 km in height, but this region is regarded as a part of the troposphere because it is generated as the result of dissipation along the surface front and, in this region, the potential temperature is so low as to remain in the troposphere even when the baroclinic disturbance is extinct.

The net transfer is summarized in Figure 16 for all applicable cases. First, the direction of the net transfer is from troposphere to stratosphere in all cases for both mass and enthalpy. The reduced scale of the troposphere is also visualized on isentropic surfaces such as those shown in Figures 3 and 7 as a diminution of the low-PV area (less than 1 PVU). As briefly summarized in *Holton et al.* [1995], the upward mass transfer agrees with previous analyses of mass transfer due to a single event of tropopause folding. Second, the net transfer is strongly sensitive to the change of stratification contrast, $S_C$. Furthermore the amount of transfer does not vary monotonically as a function of $S_C$, and the maximum transfer is obtained at the values of $S_C$ that corresponds to a realistic choice based upon modern climatology. In contrast, as the small-scale turbulence becomes stronger, the mass and heat transfer monotonically increase as expected. Nevertheless, the influence of the assumed intensity of small-scale turbulence is relatively minor in terms of the net transfer across the tropopause.

## 7. Conclusions

Idealized synoptic-scale baroclinic wave life cycles occurring along the midlatitude jet stream were simulated by employing a dry, nonhydrostatic anelastic model, and the evolution of a mini-ensemble of such events was analyzed in detail in the atmosphere-only model over a free-slip, uniform and nonheating bottom boundary. The absence in this model of an explicit parameterization of the influence of the turbulent surface boundary layer is an important caveat concerning the results we have obtained regarding the small-scale structures that develop during the course of the synoptic-scale life cycles we have analyzed. The "no-noise" initialization of well-balanced initial flow allowed us to clearly identify the distinctive and sustained period of normal mode growth with a plateau of constant growth rate, as well as the presence of an impulse of barotropic energy growth, rather than simply barotropic decay, at the termination phase of synoptic-scale development. The barotropic event was observed to occur near the northern extremum of the surface front, associated with the frontal fracture. It is also useful to note that this frontal fracture takes place prior to the onset of the viscous inhibition of frontal collapse. Although frontal collapse at the fracture point is prevented by diffusion, the temperature gradient along the warm and cold front continues to increase even after the fracture occurs except at the location of the fracture itself.

The assumed strength of the grid-scale turbulence that is represented in the model using a first-order closure with a Richardson number-dependent mixing coefficient was shown to have little influence on the deformation of the tropopause, although it significantly altered the mesoscale structures near the surface. The smoothing effect of the momentum diffusion was clearly recognized in the lower troposphere after the

decay stage of eddy kinetic energy, but the influence was minor in the stratosphere and upper troposphere according to our examination of the PV structure.

By comparing a series of simulations initialized with different degrees of stratification contrast between stratosphere and troposphere, the amplitude of the synoptic-scale deformation of the tropopause was found to be strongly sensitive to the stratification contrast, as one might expect. Although the influence of the increased contrast from the realistic level assumed in Control was minor, a large amplitude deformation was observed when the stratification contrast was reduced to 3 from the climatological value of 6. However, the behavior of the descending "tongue" of air that constitutes the tropopause fold was found to be practically insensitive to the change of the stratification contrast as if the folds were primarily associated with tropospheric dynamical processes.

The degree of irreversible (nonisentropic) mixing in the nonlinear life cycles has been evaluated by directly examining the evolution of the base potential energy. Despite the strong deformation of the tropopause, our mixing analysis showed that the baroclinic wave life cycle is essentially reversible in the sense that the irreversible change of potential energy is almost negligible compared with the reversible change of potential energy due to baroclinic stirring. However, we have made no attempt in this paper to discuss the irreversibility of the life cycle that is associated with the essentially horizontal baroclinic adjustment process which leads to a final state of the wind field that may be thought to be reached by the action of an effectively turbulent diffusivity acting in the latitudinal direction. In so far as irreversible nonisentropic or diapycnal mixing is concerned, the stratification contrast had a minor nonmonotonic influence on these flows. On the other hand, the intensity of the irreversible mixing was found to be very sensitive to the assumed intensity of turbulent diffusion, as expected. However, the change of potential energy through irreversible mixing was found to be only a few percent of that due to reversible stirring for all cases.

We have also introduced an alternative entropy-based measure of mixing. It was explicitly demonstrated that the evolution of total entropy is virtually identical to that of the base potential energy. Using the entropy-based measure of mixing, however, we have been able to clearly illustrate the fact that mixing activity occurred primarily parallel to the flow direction although there also exist regions where the structure was transverse. Despite the use of insulated free-slip surface boundary condition, the mixing activity was found to be most intense near the surface, and the longitudinal structure was found to extend vertically up to the lower stratosphere.

The response to the choice of the assumed level of small-scale turbulence was simple as expected. As we increase the parameter, more intense mixing occurs along the surface front as well as the increased exchange of mass and heat across the tropopause.

However, of all of the findings in this investigation, the most unexpected result was the complex dependence of the properties of the life cycles upon the stratification contrast, $S_C$. The surface mixing increases in the order of $S_C = 6, 4, 3,$ and 9, with the climatological value leading to the minimum mixing. Meanwhile, the amount of stratosphere-troposphere exchange increases in the order of $S_C = 3, 4, 9,$ and 6, with the climatological choice corresponding to the most intense irreversible exchange of mass and heat across the tropopause.

**References**

Añel, A. A., L. de la Torre, and L. Gimeno (2012), On the origin of air between multiple tropopauses at midlatitudes, *Sci. World J.*, *2012*, 191028, 5 pp., doi:10.1100/2012/191028.

Arakawa, A., and C. S. Konor (2009), Unification of the anelastic and quasi-hydrostatic systems of equations, *Mon. Wea. Rev.*, *137*, 710–726, doi:10.1175/2008MWR2520.1.

Bennetts, D. A., and B. J. Hoskins (1979), Conditional symmetric instability—A possible explanation for frontal rainbands, *Q. J. R. Meteorol. Soc.*, *105*, 945–962.

Boussinesq, J. (1903), *Theorie Analytique de Chaleur*, vol. 2, Gauthier-Villars, Paris.

Bush, A. B. G., and W. R. Peltier (1994), Tropopause folds and synoptic-scale baroclinic wave life cycles, *J. Atmos. Sci.*, *51*, 1581–1604.

Bush, A. B. G., J. C. McWilliams, and W. R. Peltier (1995), Origins and evolution of imbalance in synoptic-scale baroclinic wave life cycles, *J. Atmos. Sci.*, *52*, 1051–1069.

Castanheira, J. M., C. A. F. Marques, J. C. Antuña, M. L. R. Liberato, and L. Gimeno (2009), Increase of upper troposphere/lower stratosphere wave baroclinicity during the second half of the 20th century, *Atmos. Chem. Phys.*, *9*, 9143–9153. [Available at www.atmos-chem-phys.net/9/9143/2009/.]

Caulfield, C. P., and W. R. Peltier (2000), The anatomy of the mixing transition in homogeneous and stratified free shear layers, *J. Fluid Mech.*, *413*, 1–47.

Chapman, D., and K. A. Browning (1997), Rader observations of wind-shear splitting within evolving atmospheric Kelvin Helmholts billows, *Q. J. R. Meteorol. Soc.*, *123*, 1433–1439.

Chapman, D., and K. A. Browning (1999), Release of potential shearing instability in warm frontal zone, *Q. J. R. Meteorol. Soc.*, *125*, 2265–2289.

Charney, J. G. (1947), The dynamics of long waves in a baroclinic westerly current, *J. Meteorol.*, *4*, 135–162.

Chen, X., et al. (2013), The deep atmospheric boundary layer and its significance to the stratosphere and troposphere exchange over the Tibetan Plateau, *PLoS ONE*, *8*(2), e56909, doi:10.1371/journal.pone.0056909.

Clark, T. L. (1977), A small-scale dynamic model using a terrain-following coordinate transformation, *J. Comp. Phys.*, *24*, 186–215.

Danielsen, E. F., and R. S. Hipskind (1980), Stratospheric-tropospheric exchange at polar latitudes in summer, *J. Geophys. Res.*, *85*, 393–400.

Eady, E. T. (1949), Long waves and cyclone waves, *Tellus*, *1*, 33–52.

Emanuel, K. A. (1979), Inertial instability and mesoscale convective systems. Part I: Linear theory of inertial instability in rotating viscous fluids, *J. Atmos. Sci.*, *36*, 2425–2449.

Emanuel, K. A. (1988), Observational evidence of slantwise convective adjustment, *Mon. Weather Rev.*, *116*, 1805–1816.

Geng, Q., and M. Sugi (2003), Possible change of extratropical cyclone activity due to enhanced greenhouse gases and sulfate aerosols—Study with a high-resolution AGCM, *J. Clim.*, *16*, 2262–2274, doi:10.1175/1520-0442(2003)16<2262:PCOECA>2.0.CO;2.

Gettelman, A., P. Hoor, L. L. Pan, W. J. Randel, M. I. Hegglin, and T. Birner (2011), The extratropical upper troposphere and lower stratosphere, *Rev. Geophys.*, *49*, RG3003, doi:10.1029/2011RG000355.

Gill, A. E. (1982), *Atmosphere-Ocean Dynamics*, International Geophysics Series 30, Academic Press, San Diego, Calif.

Holton, J. R., P. H. Haynes, M. E. McIntyre, A. R. Douglass, R. B. Rood, and L. Pfister (1995), Stratosphere-troposphere exchange, *Rev. Geophys.*, *33*(4), 403–439, doi:10.1029/95RG02097.

Hoskins, B. J., M. E. McIntyre, and R. W. Robertson (1985), On the use and significance of isentropic potential vorticity maps, *Q. J. R. Meteorol. Soc.*, *111*, 877–946.

Haynes, P., and E. Shuckburgh (2000a), Effective diffusivity as a diagnostic of atmospheric transport: 1. Stratosphere, *J. Geophys. Res.*, *105*, 22,777–22,794.

Haynes, P., and E. Shuckburgh (2000b), Effective diffusivity as a diagnostic of atmospheric transport: 2. Troposphere and lower stratosphere, *J. Geophys. Res.*, *105*, 22,795–22,810.

Kunz, T., K. Fraedrich, and F. Lunkeit (2009), Response of idealized baroclinic wave life cycles to stratospheric flow conditions, *J. Atmos. Sci.*, *66*, 2288–2302.

Lamarque, J.-F., and P. G. Hess (1994), Cross-tropopause mass exchange and potential vorticity budget in a simulated tropopause folding, *J. Atmos. Sci.*, *51*, 2246–2269.

Langland, R. H., et al. (1999), The North Pacific Experiment (NORPEX-98): Targeted observations for improved North American weather forecasts, *Bull. Amer. Meteor. Soc.*, *80*, 1363–1384, doi:10.1175/1520-0477(1999)080<1363:TNPENT>2.0.CO;2.

Ley, B., and W. R. Peltier (1978), Wave generation and frontal collapse, *J. Atmos. Sci.*, *35*, 3–17.

Lilly, D. K. (1996), A comparison of incompressible, anelastic and Boussinesq dynamics, *Atmos. Res.*, *40*(2–4), 143–151, doi:10.1016/0169-8095(95)00031-3.

Lilly, D. K. (1962), On the numerical simulation of buoyant convection, *Tellus*, *14*, 148–172.

Lorenz, E. N. (1955), Available potential energy and the maintenance of the general circulation, *Tellus*, *7*, 157–167.

Margules, M. (1903), Über die energie der stürme. Annual volume of k.k. central institute for meteorology and terrestrial magnetism Vienna. English translation in Smithsonian Miscellaneous Collections 51, 533–595.

Mashayek, A., and W. R. Peltier (2012a), The "zoo" of secondary instabilities precursor to stratified shear flow transition. Part 1 Shear aligned convection, pairing, and braid instabilities, *J. Fluid Mech.*, *708*, 5–44.

Mashayek, A., and W. R. Peltier (2012b), The "zoo" of secondary instabilities precursor to stratified shear flow transition. Part 2 The influence of stratification, *J. Fluid Mech.*, *708*, 45–70.

Mashayek, A., and W. R. Peltier (2013), Shear-induced mixing in geophysical flows: Does the route to turbulence matter to its efficiency?, *J. Fluid Mech.*, *725*, 216–261, doi:10.1017/jfm.2013.176.

Mashayek, A., C. P. Caulfield, and W. R. Peltier (2013), Time-dependent, non-monotonic mixing in stratified turbulent shear flows: Implications for oceanographic estimates of buoyancy flux, *J. Fluid Mech.*, *736*, 570–593, doi:10.1017/jfm.2013.551.

Methven, J. (1998), Spirals in potential vorticity. Part II: Stability, *J. Atmos. Sci.*, *55*, 2067–2079.

Methven, J., and B. J. Hoskins (1998), Spirals in potential vorticity. Part I: Measures of structure, *J. Atmos. Sci.*, *55*, 2053–2066.

Molemaker, M. J., J. C. McWilliams, and I. Yavneh (2005), Baroclinic instability and loss of balance, *J. Phys. Oceanogr.*, *35*, 1505–1517, doi:10.1175/JPO2770.1.

Moon, W., and S. B. Feldstein (2009), Two types of baroclinic life cycles during the Southern Hemisphere summer, *J. Atmos. Sci.*, *66*, 1401–1427.

Munk, W. (1966), Abyssal recipes, *Deep-Sea Res.*, *13*, 707–730.

Munk, W., and C. Wunsch (1998), Abyssal recipes II: Energetics of tidal and wind mixing, *Deep Sea Res., Part I*, *45*, 1997–2010.

Nakamura, N. (1996), Two-dimensional mixing, edge formation, and permeability diagnosed in an area coordinate, *J. Atmos. Sci.*, *53*, 1524–1537.

Nakamura, N. (2001), A new look at eddy diffusivity as a mixing diagnostic, *J. Atmos. Sci.*, *58*, 3685–3701.

Nakamura, N., and A. Solomon (2011), Finite-amplitude wave activity and mean flow adjustments in the atmospheric general circulation. Part II: Analysis in the isentropic coordinate, *J. Atmos. Sci.*, *68*, 2783–2799.

Neiman, J. P., M. A. Shapiro, and L. S. Fedor (1993), The life cycle of an extratropical marine cyclone. Part II: Mesoscale structure and diagnostics, *Mon. Weather Rev.*, *121*, 2177–2199.

Osborn, T. R. (1980), Estimates of the local rate of vertical diffusion from dissipation measurements, *J. Phys. Oceanogr.*, *10*, 83–89.

O'Sullivan, D., and T. J. Dunkerton (1995), Generation of inertia gravity waves in a simulated life cycle of baroclinic instability, *J. Atmos. Sci.*, *52*, 3695–3716.

Patmore, N., and R. Toumi (2006), Entropy-based measure of mixing at the tropopause, *Q. J. R. Meteorol. Soc.*, *132*, 1949–1976, doi:10.1256/qj.05.84.

Peltier, W. R., and C. P. Caulfield (2003), Mixing efficiency in stratified shear flows, *Annu. Rev. Fluid Mech.*, *35*, 135–67, doi:10.1146/annurev.fluid.35.101101.161144.

Plougonven, R., and C. Snyder (2007), Inertia-gravity waves spontaneously generated by jets and fronts. Part I: Different baroclinic life cycles, *J. Atmos. Sci.*, *64*, 2502–2520.

Polavarapu, S. M., and W. R. Peltier (1990), The structure and nonlinear evolution of synoptic-scale cyclones: Life-cycle simulations with a cloud-scale model, *J. Atmos. Sci.*, *47*, 2645–2672.

Polavarapu, S. M., and W. R. Peltier (1993), Formation of small-scale cyclones in numerical simulations of synoptic scale baroclinic wave life cycles: Secondary instability at the cusp, *J. Atmos. Sci.*, *50*, 1047–1057.

Polvani, L. M., and J. G. Esler (2007), Transport and mixing of chemical air masses in idealized baroclinic life cycles, *J. Geophys. Res.*, *112*, D23102, doi:10.1029/2007JD008555.

Raymond, D. J. (1978), Instability of the low-level jet and severe storm formation, *J. Atmos. Sci.*, *35*, 2274–2280.

Shapiro, M. A., and D. Keyser (1990), Fronts, jet streams, and tropopause, in *Extratropical Cyclones: The Erik Palmén Memorial Volume*, edited by C. W. Newton and E. O. Holopainen, pp. 167–191, Am. Meteorol. Soc., Boston, Mass.

Simmons, A. J., and B. J. Hoskins (1977), Baroclinic instability on the sphere: Solutions with a more realistic tropopause, *J. Atmos. Sci.*, *34*, 581–588.

Simmons, A. J., and B. J. Hoskins (1978), The life cycles of some nonlinear baroclinic waves, *J. Atmos. Sci.*, *35*, 414–432.

Stohl, A., et al. (2003), Stratosphere-troposphere exchange: A review, and what we have learned from STACCATO, *J. Geophys. Res.*, *108*(D12), 8516, doi:10.1029/2002JD002490.

Thorncroft, C. D., B. J. Hoskins, and M. E. McIntyre (1993), Two paradigms of baroclinic-wave life-cycle behaviour, *Q. J. R. Meteorol. Soc.*, *119*, 17–55, doi:10.1002/qj.49711950903.

Thorpe, S. A. (1977), Turbulence and mixing in a Scottish lock, *Phil. Trans. R. Soc. A*, *286*, 125–181, doi:10.1098/rsta.1977.0112.

Wang, S., and L. M. Polvani (2011), Double tropopause formation in idealized baroclinic life cycles: The key role of an initial tropopause inversion layer, *J. Geophys. Res.*, *116*, D05108, doi:10.1029/2010JD015118.

Wakimoto, R. M., and B. Bosart (2001), Airborne radar observations of a warm front during FASTEX, *Mon. Weather Rev.*, *129*, 254–274.

Winters, K. B., P. N. Lombard, J. J. Riley, and E. A. D'Asaro (1995), Available potential energy and mixing in density-stratified fluids, *J. Fluid Mech.*, *289*, 115–128, doi:10.1017/S002211209500125X.

World Meteorological Organization (1957), Meteorology—A three-dimensional science: Second session of the commission for aerology, WMO Bulletin IV(4), WMO, Geneva, 134–138.

Yamazaki, Y. H., and W. R. Peltier (2001), The existence of subsynoptic-scale baroclinic instability and the nonlinear evolution of shallow disturbances, *J. Atmos. Sci.*, *58*, 657–683, doi:10.1175/1520-0469(2001)058<0657:TEOSSB>2.0.CO;2.

Yamazaki, Y. H., D. R. Skeet, and P. L. Read (2004), A new general circulation model of Jupiter's atmosphere based on the UKMO Unified Model: Three-dimensional evolution of isolated vortices and zonal jets in mid-latitudes, *Planet. Space Sci.*, *52*, 423–445, doi:10.1016/j.pss.2003.06.006.